

A photochemical model for the Venus atmosphere at 47–112 km

Vladimir A. Krasnopolsky*

Department of Physics, Catholic University of America, Washington, DC 20064, United States
 Moscow Institute of Physics and Technology, Dolgoprudny 141700, Russia

ARTICLE INFO

Article history:

Received 22 July 2011

Revised 26 October 2011

Accepted 10 November 2011

Available online 28 November 2011

Keywords:

Venus

Venus, Atmosphere

Photochemistry

Atmospheres, Composition

Atmospheres, Chemistry

ABSTRACT

The model is intended to respond to the recent findings in the Venus atmosphere from the Venus Express and ground-based submillimeter and infrared observations. It extends down to 47 km for comparison with the kinetic model for the lower atmosphere (Krasnopolsky, V.A. [2007]. *Icarus* 191, 25–37) and to use its results as the boundary conditions. The model numerical accuracy is significantly improved by reduction of the altitude step from 2 km in the previous models to 0.5 km. Effects of the NUV absorber are approximated using the detailed photometric observations at 365 nm from Venera 14. The H₂O profile is not fixed but calculated in the model. The model involves odd nitrogen and OCS chemistries based on the detected NO and OCS abundances. The number of the reactions is significantly reduced by removing of unimportant processes. Column rates for all reactions are given, and balances of production and loss may be analyzed in detail for each species.

The calculated vertical profiles of CO, H₂O, HCl, SO₂, SO, OCS and of the O₂ dayglow at 1.27 μm generally agree with the existing observational data; some differences are briefly discussed. The OH dayglow is ~30 kR, brighter than the OH nightglow by a factor of 4. The H + O₃ process dominates in the nightglow excitation and O + HO₂ in the dayglow, because of the reduction of ozone by photolysis. A key feature of Venus' photochemistry is the formation of sulfuric acid in a narrow layer near the cloud tops that greatly reduces abundances of SO₂ and H₂O above the clouds. Delivery of SO₂ and H₂O through this bottleneck determines the chemistry and its variations above the clouds. Small variations of eddy diffusion near 60 km result in variations of SO₂, SO, and OCS at and above 70 km within a factor of ~30. Variations of the SO₂/H₂O ratio at the lower boundary have similar but weaker effect: the variations within a factor of ~4 are induced by changes of SO₂/H₂O by ±5%. Therefore the observed variations of the mesospheric composition originate from minor variations of the atmospheric dynamics near the cloud layer and do not require volcanism. NO cycles are responsible for production of a quarter of O₂, SO₂, and Cl₂ in the atmosphere. A net effect of photochemistry in the middle atmosphere is the consumption of CO₂, SO₂, and HCl from and return of CO, H₂SO₄, and SO₂Cl₂ to the lower atmosphere. These processes may be balanced by thermochemistry in the lower atmosphere even without outgassing from the interior, though the latter is not ruled out by our models. Some differences between the model and observations and the previous models are briefly discussed.

© 2011 Elsevier Inc. All rights reserved.

1. Introduction: History and the current state of the problem

Photochemical modeling is a powerful tool to study chemical compositions of the planetary atmospheres. Using densities of a few parent species at a lower boundary, it makes it possible to calculate vertical profiles of dozens of species throughout the atmosphere. The atmosphere of Venus covers a wide range of temperature and pressure, has a complicated chemical composition, and its chemical modeling is a challenging task.

* Address: Department of Physics, Catholic University of America, Washington, DC 20064, United States.

E-mail address: vlad.krasn@verizon.net

Five years have passed since the beginning of the science phase of the European Venus Express mission. Numerous data on the chemical composition have been obtained in the altitude range of our interest. These data include vertical profiles of H₂O and HDO (Fedorova et al., 2008), CO, HCl, and HF (Vandaele et al., 2008), SO and SO₂ (Belyaev et al., 2008, 2012) that are measured using SPICAV/SOIR (Bertaux et al., 2007) in the solar occultation mode. Variations of SO₂ and CO near the cloud tops were studied by SPICAV in the nadir mode (Marcq et al., 2011) and VIRTIS (Irwin et al., 2008), respectively. Discoveries of the OH nightglow (Piccioni et al., 2008; Soret et al., 2010) and the NO nightglow at 1.22 μm (Garcia Munoz et al., 2009a), detailed observations of the O₂ nightglow at 1.27, 1.58 μm (Piccioni et al., 2009), and in the visible range (Garcia Munoz et al., 2009b) and the NO UV nightglow (Gerard

et al., 2008) are also related to the chemical composition of the Venus atmosphere and reflect the global thermospheric dynamics.

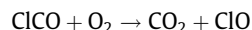
Ground-based observations in the submillimeter range reveal large-scale variations of temperature and CO (Clancy et al., 2012), H₂O (Sandor and Clancy, 2005), SO₂ and SO (Sandor et al., 2010), and a restrictive upper limit to H₂SO₄ vapor (Sandor et al., 2012). These observations cover the altitude range of 70–110 km. The achieved spectral resolving power is very high ($\sim 10^7$), and analyses of the observed line shapes give some data on the vertical distributions of the observed species.

Ground-based spatially-resolved high-resolution spectroscopy in the near infrared resulted in detections of NO (Krasnopolsky, 2006a) and OCS (Krasnopolsky, 2008) at the cloud tops. Latitudinal and local time (from morning to late afternoon) variations of the cloud deck, CO, HCl, HF, HDO, SO₂, and OCS at the cloud tops (Krasnopolsky, 2010b,c) were measured as well. The visible nightglow was observed by Slinger et al. (2006), the O₂ nightglow at 1.27 μ m and its temperature were measured by Ohtsuki et al. (2008), Bailey et al. (2008), and Krasnopolsky (2010a) who also detected the OH nightglow.

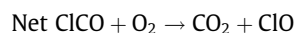
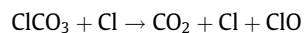
Here we do not consider spacecraft and ground-based observations of the Venus chemical composition below the clouds. The above list does not also include numerous and important data published before 2000.

Photochemical modeling of the Venus atmosphere has a long history, and Prinn (1971) was the first who recognized the importance of ClO_x chemistry on Venus. That was done before this chemistry was understood in the Earth's atmosphere. Krasnopolsky and Parshev (1981, 1983) calculated a photochemical model with a ClCO cycle and related ClCO chemistry that dominate in recombination of CO with O and O₂ on Venus.

Yung and DeMore (1982) argued that the reaction



from the model by Krasnopolsky and Parshev proceeds in two steps:



with the same net result, and this was later confirmed in the laboratory (Pernice et al., 2004). Yung and DeMore (1982) suggested three models based on abundant H₂ (model A), NO with a mixing ratio of 30 ppb produced by lightning in model B, and the ClCO cycle in models B and C. Observations have not confirmed the assumptions of models A and B, and model C was the basic model and was further developed by Mills (1998). The model by Mills (1998) was not published but is accessible as a PhD thesis. A modified version of the model by Mills (1998) was suggested by Mills and Allen (2007). They did not fix CO at the lower boundary of 58 km as it was done in the previous models, and the calculated CO near the cloud tops was much smaller than the measured values.

Recently Zhang et al. (2010) calculated photochemical models to fit very large abundances of SO₂ ~ 1 ppm at 100–110 km from the SPICAV-UV solar occultations. However, detailed analysis of the SO₂ and SO profiles from the SPICAV-UV and SOIR solar occultations became available only recently (Belyaev et al., 2012) after the submission of this work and simultaneously with an updated version of the photochemical model (Zhang et al., 2012). This model adopted many (but not all) elements of Mills (1998).

Our objective in this paper is to develop a global-mean photochemical model for the middle atmosphere of Venus that reflects the new observational results and the current state of chemical kinetics related to the problem. The model results will be com-

pared with the observations and the models by Mills (1998), Mills and Allen (2007), and Zhang et al. (2012).

2. Input data of the model

Here we will briefly discuss main features of our model and consider in more detail some differences between our and previous models. Our approach is to remove from the model all species and reactions that are not essential and do not affect abundances of the observable species and those that may become observable. The basic input data are the Venus orbit radius of 0.72 AU, its surface radius and gravity acceleration of 6052 km and 887 cm s⁻², respectively, and the mean molecular mass of 43.44 atomic units.

2.1. Altitude range and step

The models by Yung and DeMore (1982), Mills (1998), Mills and Allen (2007), and Zhang et al. (2010, 2012) were calculated for the altitude range of 58–112 km with a step of 2 km. (Zhang et al. (2012) used steps of 0.4 km at 58–60 km.) The upper boundary of 112 km allows neglecting molecular diffusion and ion chemistry. Effects of chemistry of the upper atmosphere and ionosphere may be simulated by fluxes of O, O₂, CO, and N at the upper boundary, while the basic photochemical processes occur below 112 km.

The lower boundary at 58 km is near the transition between the upper and middle cloud layers. The UV radiation is completely absorbed above this height while the temperature is still rather low to initiate thermochemical reactions. Therefore, this choice is justified as well. However, we change the lower boundary in our model and move it to the lower cloud boundary near 47 km. This height is the upper boundary in the chemical kinetic model for the Venus lower atmosphere (Krasnopolsky, 2007), and some results of that model may be used as the lower boundary conditions in our model.

Accuracy of finite difference schemes for the 1D-photochemical modeling depends on a vertical step d . Considering a species with no photochemical sources and sinks, a true reduction in density per a vertical step d , $e^{-d/H}$, is substituted by $1 - d/H$ in the finite difference schemes. Here H is the density scale height, and its mean value is 4.9 km for 47–112 km and 4.5 km for 58–112 km. Then the true density at the upper boundary h_u is $n_u = n_0 e^{-\frac{h_u-h_0}{H}}$, while the finite difference scheme gives $n_u = n_0(1 - d/H)^{(h_u-h_0)/d}$. An error accumulated from the bottom h_0 to the top h_u is a factor of

$$e^{(h_u-h_0)/H} (1 - d/H)^{(h_u-h_0)/d}.$$

This factor is equal to 0.48, 0.21, and 0.023 for the step $d = 0.5$, 1, and 2 km, respectively. The factors are slightly worse (0.47, 0.19, and 0.020, respectively) if the true variable scale height is used instead of the mean value. The term $1 - d/H$ is changed to $2 - d/H_i - T_{i+1}/T_i$ in this case, and H_i is the local scale height for pressure.

The error in the species mixing ratio is compensated, if both the species and CO₂ are calculated by the finite difference scheme. However, the number densities of both CO₂ and the species at the upper boundary are significantly underestimated in this case. The error at the boundaries may be reduced if the CO₂ density is corrected to fit a value in the middle of the altitude range: the factors are 0.7, 0.46, and 0.15, respectively, in this case. Evidently the above consideration for a species without chemical sources and sinks is valid for all species, though the proof is more complicated in this general case. The computation time is proportional to $\sim d^{-1}$ and longer for the small steps. However, the reduction of the altitude step from 2 km to 0.5 km significantly improves the numerical accuracy of the model, and our models in Krasnopolsky (2010a) and here are calculated with $d = 0.5$ km.

2.2. Temperature and eddy diffusion

The temperature profile for our model (Fig. 1) is taken from VIRA (Seiff et al., 1985) for latitude of 45°. The temperatures at 100–112 km are from the dayside VIRA (Keating et al., 1985). Density at 47 km of $3.6 \times 10^{19} \text{ cm}^{-3}$ is chosen to fit the VIRA density at 74 km (see the previous section), while the VIRA density at 47 km is $3.0 \times 10^{19} \text{ cm}^{-3}$.

Eddy diffusion is assumed constant at $K = 10^4 \text{ cm}^2 \text{ s}^{-1}$ below a breakpoint h_e and at $K = 10^7 \text{ cm}^2 \text{ s}^{-1}$ above 100 km. Eddy diffusion increases exponentially between these two points (Fig. 1). Variations of K above 100 km weakly affect the solution; however, it is very sensitive to variations of K below 70 km. The breakpoint h_e is at 60 km in our basic model and at 55 and 65 km in auxiliary models and sensitivity tests (Fig. 1). Eddy diffusion exceeds molecular diffusion for all species by more than an order of magnitude even at the upper boundary, and molecular diffusion may be safely neglected in our model.

Eddy diffusion was estimated using the He/CO₂ ratio above 130 km observed by the PV bus mass spectrometer (von Zahn et al., 1980), altitude profiles of the haze observed from the V9, V10 (Krasnopolsky, 1980, 1983) and PV (Lane and Optsbaum, 1983) orbiters, profile of the mode 1 particles (Krasnopolsky, 1985), and fluctuations of signal in the radio occultations (Woo and Ishimaru, 1981). A summary of these data is shown in Fig. 1 along with the adopted profile of eddy diffusion, which is in reasonable agreement with the data.

2.3. Absorption of the solar radiation and the NUV absorber

The solar UV radiation in the range of 120–410 nm is taken from Woods et al. (1996) and interpolated to intermediate solar conditions, corresponding to $F_{10.7\text{cm}} = 150$. The dayside mean $\cos z$ is 0.5 (z is the solar zenith angle), and the solar flux scaled to the Venus orbit is halved to account for diurnal averaging in the global mean model. These factors are compensating, and the solar flux at 1 AU with $\cos z = 0.5$ is used for our models.

Extinction of the sunlight in the atmosphere of Venus is caused mainly by CO₂, SO₂, the NUV absorber, and scattering processes in the Venus clouds. Basic data on the vertical distribution of the NUV absorber were obtained from a scanning photometer at the Venera 14 descent probe (Economov et al., 1983). The photometer band-

width was 70 nm centered at 365 nm, and the radiation was measured during the descent from zenith, nadir, and four other directions. The retrieved true absorption coefficient steeply decreased by a factor of 20 from 60 km to a minimum near 57 km and then gradually increased to the lower cloud boundary at 48 km by a factor of 10. The NUV absorber is responsible for the absorption above 58 km, and the growth to 48 km is caused by SO₂ (Economov et al., 1983) with a mixing ratio increasing from 10 ppm at 57 km to 50 ppm at 50 km (Krasnopolsky, 1986, p. 152).

The photon fluxes directly measured by Venera 14 are integrated over the sphere to calculate photolysis rates. The integration over the sphere partly compensates for the absorption: for example, scattering by a uniform cloud layer with the lambertian reflectivity a increases a photolysis rate above the clouds by a factor of $1 + 2a$. We find that the complicated processes of scattering and absorption may be approximated by a uniform pure absorbing layer at 58–67 km with $\tau \approx 0.5$. This layer is extended above 67 km with a scale height of 3 km. This approximation is used to simulate the illumination profile at 365 nm. A wavelength behavior of the NUV absorption is unknown, and we adopt it equal to that at 365 nm times $\exp((\lambda_{\text{nm}} - 365)/100)$, i.e., the absorption depth decreases with wavelength by a factor of $e = 2.72$ per 100 nm. The absorption extends to 400 nm in our model.

Mills (1998), Mills and Allen (2007), and Zhang et al. (2010, 2012) made radiative transfer calculations and adopted the NUV absorber properties suggested by Crisp (1986) and based on the NUV reflectivity of Venus and the PV photometer data in the red. Crisp (1986) assumed that the NUV absorption disappears below 310 nm, where the SO₂ absorption dominates. However, usually UV continuum absorption extends to very short wavelengths below the absorption limit. FeCl₃ in the sulfuric acid aerosol, suggested as a NUV absorber (Zasova et al., 1981; Krasnopolsky, 1985) is not considered in our model. Consequently, the absorption effect is simulated by the above approximation.

2.4. Water vapor

The vertical profile of H₂O was fixed at 1 ppm in the models by Yung and DeMore (1982), in excellent agreement with the SOIR observations at 70–110 km made a quarter of century later (Fedorova et al., 2008). This profile was fixed at 0.5 ppm up to 80 km with a steep decrease above 80 km in Mills (1998), Mills and Allen (2007), and Zhang et al. (2010). Zhang et al. (2012) adopted an H₂O profile also from the SOIR observations (Bertaux et al., 2007), and it is nearly constant at 1 ppm throughout 58–112 km.

However, selfconsistent photochemical models require calculations of the vertical profiles of species involved. Therefore the H₂O profile is calculated in our model with a boundary condition of 21 ppm at 47 km from the model by Krasnopolsky (2007). That model applied 30 ppm of H₂O as a boundary condition near the surface, and the calculated abundances of H₂O and H₂SO₄ vapors are 21 and 9 ppm, respectively, at 47 km. Those results agree with the element conservation (Krasnopolsky, 1986, 1995). The adopted 30 ppm of H₂O in the lowest scale height was based on Pollack et al. (1993) and was recently confirmed by the SPICAV-IR observations (Bezard et al., 2011).

We will see below that the formation of almost all sulfuric acid occurs in a narrow layer that peaks at 66 km near the cloud tops, where the concentration is equal to 85% (Krasnopolsky, 2007). The widespread value of 75% (see e.g. Zhang et al., 2010) for the sulfuric acid concentration at the cloud tops is incompatible with spectroscopic data and requires the H₂O mixing ratio of ~ 25 ppm at 68 km that is not supported by the observations. The concentration of 85% corresponds to the proportion of monohydrate H₂SO₄·H₂O, that is, two H₂O molecules are lost per each molecule of sulfuric acid. Therefore we assume that sulfuric acid forms as

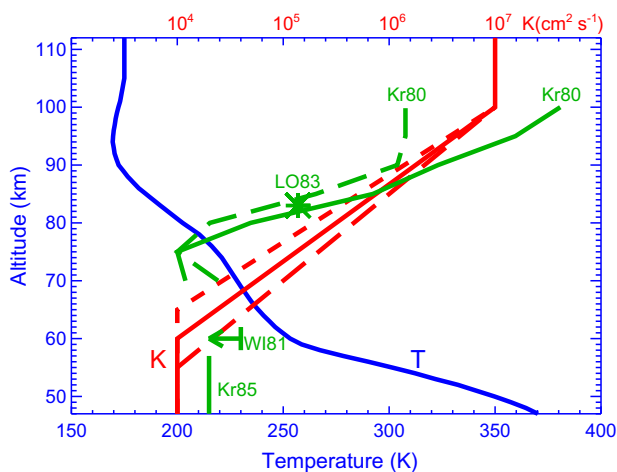


Fig. 1. Profiles of temperature and eddy diffusion in the model. Data on eddy diffusion retrieved from observations of aerosol (Krasnopolsky, 1980, 1983, 1985; Lane and Optsbaum, 1983) and scintillations of radio signal (upper limit, Woo and Ishimaru, 1981) are also shown (green). (For interpretation of the references to color in this figure legend, the reader is referred to the web version of this article.)

the monohydrate and neglect further interaction between water vapor and sulfuric acid in our model.

2.5. H_2SO_4 vapor

SPICAV-UV and SOIR occultations (Belyaev et al., 2012) result in vertical profiles of SO_2 at 70–105 km and SO at 90–105 km. The observed mean SO_2 abundances are ~ 300 ppb near 100 km and exceed those near 80 km. Ground-based submillimeter observations (Sandor et al., 2010) revealed mean SO_2 and SO mixing ratios of 23 and 7.5 ppb, respectively, at 84–100 km, decreasing below 84 km. Though the retrieved abundances are smaller than the VEX data by an order of magnitude, both sets of the observations require a source of SO_X near 100 km.

Zhang et al. (2010) calculated models with photolysis of H_2SO_4 vapor above 90 km as a high-altitude source of SO_X . They adopted the highest midnight temperatures that reach 250 K at 96 km. These temperatures were measured by SPICAV-UV stellar occultations (Bertaux et al., 2007). They also assumed that the haze above 90 km consists of the pure sulfuric acid and H_2SO_4 vapor is supersaturated by a factor of 10. Furthermore, they adopted the H_2SO_4 - H_2O photolysis frequency that exceeded the H_2SO_4 value by a factor of 100, though abundance of the monohydrate is negligible in the vapor above the pure sulfuric acid. Then the H_2SO_4 vapor mixing ratio reached 10 ppm at 96 km, and the column production of SO_X by photolysis of H_2SO_4 was $2.8 \times 10^{10} \text{ cm}^{-2} \text{ s}^{-1}$ above 90 km (Table 1).

Similar to their previous model, Zhang et al. (2012) applied the midnight temperature profile from Bertaux et al. (2007); however, H_2SO_4 vapor was undersaturated in their basic model by a factor of 4. They assumed that the H_2SO_4 photolysis cross-sections at 195–330 nm are equal to the established upper limit of 10^{-21} cm^2 . This assumption increased the H_2SO_4 photolysis frequency by two orders of magnitude, similar to that of H_2SO_4 - H_2O in their previous model; however, this assumption does not contradict the existing facts. The H_2SO_4 vapor mixing ratio peaks at 200 ppb, and the H_2SO_4 column photolysis rate is $10^9 \text{ cm}^{-2} \text{ s}^{-1}$ above 90 km (Table 1).

The vertical profiles of H_2SO_4 vapor were **adopted** in both above models by scaling the saturated densities of H_2SO_4 vapor above the pure sulfuric acid at the midnight temperatures from Bertaux et al. (2007). Krasnopolsky (2011b) **calculated** a profile of H_2SO_4 vapor by solving the continuity equations that account for condensation and sublimation of H_2O and H_2SO_4 vapors, their photolyses, and vertical transport by eddy diffusion. He argued that the temperatures ~ 250 K near 96 km disagree with rotational temperature of the O_2 nightglow at $1.27 \mu\text{m}$ that is equal to 187 ± 3 K in observations by five independent teams. A radiative lifetime is 1.2 h for this nightglow, and its peak is at 95–100 km, so that the rotational temperature should be similar to the kinetic temperature near 96 km. The temperatures of ~ 250 K disagree with the radiooccultation and infrared observations at 15 and $4.3 \mu\text{m}$ as well. Furthermore, the nighttime conditions are inapplicable to the H_2SO_4 photolysis that occurs on the day side. The calculated abundances and photolysis rates of H_2SO_4 vapor in Krasnopolsky (2011b) are

smaller than those adopted in Zhang et al. (2010, 2012) by many orders of magnitude (Table 1).

Attempts to detect H_2SO_4 vapor in the submillimeter range (Sandor et al., 2012) resulted in an upper limit of 3 ppb to H_2SO_4 vapor at 85–100 km. It looks much smaller than the peak abundances of 10 ppm and 200 ppb in Zhang et al. (2010, 2012); however, the column abundances at 85–100 km correspond to 300 and 10 ppb, respectively, still above the upper limit (Table 1). Based on the results in Krasnopolsky (2011b) and Sandor et al. (2012), we will neglect the photolysis of H_2SO_4 vapor in our model.

2.6. Elemental sulfur

Sulfur vapor consists of eight allotropes S_X , $X = 1-8$. Its composition for thermodynamic equilibrium at 300 K is given in Table 2 using the data from Mills (1974) and Lyons (2008). Both compilations are based on the laboratory studies in 1960–1970s that were made at $T > 320$ K. Extrapolation to the lower temperatures involves three terms in Mills (1974) and two terms in Lyons (2008). There are significant differences between the results.

The existing kinetic data refer to (R120) $S + S + M$ and (R122) $S_2 + S_2 + M$. Fair and Thrush (1969) measured $k_{120} = 2.8 \times 10^{-33} \text{ cm}^6 \text{ s}^{-1}$ for $M = \text{Ar}$ at 300 K, while Nicholas et al. (1979) found $k_{120} = 1.2 \times 10^{-29} \text{ cm}^6 \text{ s}^{-1}$ for $M = H_2S$ at 300 K. The difference by four orders of magnitude can hardly be explained by the different third bodies. Calculations by Du et al. (2008) agree with the result of Fair and Thrush (1969), and we apply k_{120} from Du et al. (2008) corrected for the greater efficiency of $M = CO_2$. The only measurement of k_{122} (Nicholas et al., 1979) is rather similar to their k_{120} , and we adopt the value of k_{120} for all three-body associations of the sulfur allotropes in our model.

Mills (1998) suggested 21 reactions between the sulfur allotropes. Moses et al. (2002) considered 47 reactions between these species on Io. However, both systems fail to simulate the much smaller densities of S_4 than those of S_5 to S_8 (Table 2). For example, densities of all allotropes are equal to $\sim 10^8 \text{ cm}^{-3}$ at 60 km in Mills (1998). S_4 is more abundant than S_5 to S_8 at 62 km in Zhang et al. (2012) who adopted the S_X reactions from Moses et al. (2002). Model B in Zhang et al. (2012) adopted the saturated vapor densities of S_X from Lyons (2008) at the temperatures from Bertaux et al. (2007) scaled by a factor of 3×10^{-4} . However, these highly undersaturated densities significantly exceed the saturated densities at the true temperatures ~ 180 K. The SO_X production in model B from reactions of atomic oxygen with the adopted S_X vapors was $4 \times 10^8 \text{ cm}^{-2} \text{ s}^{-1}$ above 90 km, smaller than the H_2SO_4 photolysis in model A by a factor of 2.5.

We conclude that the chemical kinetics between S_X needs special study to fit the thermodynamic data, and this study is beyond the current work. Here we consider three sulfur allotropes S , S_2 , and S_3 and assume that all $S_{X>3}$ form aerosol particles with radius of $0.5 \mu\text{m}$ and density of $\sim 2 \text{ g cm}^{-3}$. This is a mean particle radius observed by the V9–10 near 73 km (Krasnopolsky, 1980, 1983), and the adopted density is close to that of solid sulfur. These particles react with atomic oxygen to form SO (R127) and precipitate with the Stokes velocity. Reaction probability in the collisions

Table 1

H_2SO_4 vapor above 85 km adopted in models by Zhang et al. (2010, 2012), calculated by Krasnopolsky (2011b), and observed by Sandor et al. (2012, bold).

Parameter	Zhang et al. (2010) ^a	Krasnopolsky (2011b)	Sandor et al. (2012)	Zhang et al. (2012) ^b
$f_{H_2SO_4}$, 96 km	10^{-5}	7×10^{-14}	–	2×10^{-7}
H_2SO_4 (cm^{-2} , 85–100 km)	6×10^{15}	3×10^8	$< 6 \times 10^{13}$	2×10^{14}
$f_{H_2SO_4}$, 85–100 km	3×10^{-7}	10^{-14}	$< 3 \times 10^{-9}$	10^{-8}
Photolysis frequency (s^{-1})	5×10^{-6}	5×10^{-8}	–	7×10^{-6}
Photolysis rate ($\text{cm}^{-2} \text{ s}^{-1}$, 90 km)	2.8×10^{10}	23	–	10^9

^a Model C.

^b Model A.

Table 2
Composition of sulfur vapor for thermodynamic equilibrium at 300 K.

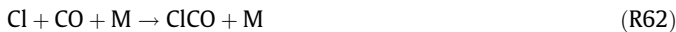
	S ₂	S ₃	S ₄	S ₅	S ₆	S ₇	S ₈
Mills (1974)	3.6 + 5	2600	0.001	2.0 + 8	1.7 + 10	9.57 + 9	1.5 + 11
Lyons (2008)	2.4 + 4	2200	3700	1.3 + 7	5.6 + 9	1.6 + 9	9.5 + 10

The S_X number densities are in cm⁻³; 3.6 + 5 = 3.6 × 10⁵.

between O and S₂ is ~0.1, and we estimate an uptake coefficient in the collisions between O and aerosol sulfur at 0.01. The sulfur particles are a minor component of the Venus aerosol, and their size and the uptake coefficient are poorly known. However, our model is weakly sensitive to these values.

2.7. Balance of CICO

The CICO chemistry is almost completely responsible for recombination of CO₂ in the middle atmosphere of Venus. Densities of CICO are determined by a balance of the direct and inverse reactions:



Rate coefficients of the direct reaction for M = N₂ measured by Clark et al. (1966), Nicovich et al. (1990), and Hewitt et al. (1996) are equal to (1.1, 1.6, and 1.3) × 10⁻³³ cm⁶ s⁻¹, respectively, at 300 K. According to Nicovich et al. (1990), the third-body efficiency

Table 3
Species calculated in the model.

CO ₂ , CO, O, O ⁺ , O ₂ , O ₂ ⁺ , O ₃ , H ₂ O, H, OH, HO ₂ , H ₂ , SO ₂ , OCS, SO, SO ₃ , HSO ₃ , H ₂ SO ₄ , S, S ₂ , S ₃ , S ₄ , S ₂ O, S ₂ O ₂ , HCl, Cl, ClO, ClO ₂ , Cl ₂ , CICO, CICO ₃ , COCl ₂ , OSCI, SCl, SCl ₂ , ClSO ₂ , SO ₂ Cl ₂ , N, NO, NO ₂ , NO ₃ , ClNO, HO ₂ NO ₂ , SNO
--

O⁺ = O(¹D), O₂⁺ = O₂(a¹Δ_g).

Table 4
Reactions of photodissociation.

#	Reaction	Reference and photolysis frequency	Column rate	h (km)
1	CO ₂ + hν → CO + O	Shemansky (1972), Parkinson et al. (2003)	4.03 + 12	88
2	CO ₂ + hν → CO + O ⁺	λ < 167 nm; Lewis and Carver (1983)	6.65 + 10	110
3	SO ₂ + hν → SO + O	Prahlad and Kumar (1997), Manatt and Lane (1993)	1.02 + 13	72
4	O ₂ + hν → O + O	Nair et al. (1994)	1.20 + 10	89
5	O ₂ + hν → O ⁺ + O	Nair et al. (1994)	1.91 + 9	106
6	O ₃ + hν → O ₂ ⁺ + O ⁺	0.0085; Sander et al. (2011)	1.52 + 12	80
7	SO ₃ + hν → SO ₂ + O	Burkholder and McKeen (1997)	4.66 + 9	70
8	SO + hν → S + O	Phillips (1981)	6.08 + 11	79
9	OCS + hν → CO + S	Molina et al. (1981)	7.12 + 10	59
10	S ₂ O + hν → SO + S	0.04; Mills (1998)	7.97 + 9	70
11	S ₂ + hν → S + S	6 × 10 ⁻³ ; Mills (1998)	4.85 + 7	61
12	S ₃ + hν → S ₂ + S	1.37γ; Billmers and Smith (1991); γ = 0.1 assumed	9.76 + 5	58
13	S ₂ O ₂ + hν → SO ₂ + S	0.01; see text	1.82 + 12	70
14	H ₂ O + hν → OH + H	Cheng et al. (1999)	1.30 + 9	95
15	HCl + hν → H + Cl	Bahou et al. (2001)	9.46 + 10	74
16	ClO + hν → Cl + O	0.0065; Sander et al. (2011)	5.17 + 11	75
17	ClO ₂ + hν → ClO + O	0.009; Sander et al. (2011)	7.10 + 7	79
18	CICO ₃ + hν → CO ₂ + ClO	0.0032; Pernice et al. (2004)	7.90 + 10	76
19	Cl ₂ + hν → Cl + Cl	0.0026; Sander et al. (2011)	3.18 + 13	71
20	SCl + hν → S + Cl	0.05; Mills (1998)	1.03 + 10	70
21	SCl ₂ + hν → SCl + Cl	0.005; Mills (1998)	3.04 + 9	70
22	COCl ₂ + hν → CICO + Cl	4 × 10 ⁻⁵ ; Sander et al. (2011)	2.82 + 8	71
23	NO + hν → N + O	Allen and Frederick (1982)	1.02 + 7	83
24	NO ₂ + hν → NO + O	0.01; Sander et al. (2011)	1.49 + 12	70
25	NO ₃ + hν → NO ₂ + O	0.16; Sander et al. (2011)	5.26 + 10	70
26	NO ₃ + hν → NO + O ₂	0.02; Sander et al. (2011)	6.58 + 9	70
27	HO ₂ NO ₂ + hν → HO ₂ + NO ₂	4.3 × 10 ⁻⁴ ; Sander et al. (2011)	1.85 + 8	66
28	ClNO + hν → Cl + NO	0.005; Sander et al. (2011)	1.63 + 11	66
29	SNO + hν → S + NO	0.01 = J ₂₄	1.06 + 11	59
30	SO ₂ Cl ₂ + hν → ClSO ₂ + Cl	1.6 × 10 ⁻⁴ ; Uthman et al. (1978)	2.31 + 12	66

Numerical values of photolysis frequencies are in s⁻¹ for λ > 200 nm at 1 AU. Column rates are in cm⁻² s⁻¹; h is the weighted-mean altitude of a reaction.

ratio is CO₂:N₂:CO:Ar = 3.2:1:1:0.8, and the value for Ar in Clark et al. (1966) is corrected for this ratio. A temperature dependence of the rate coefficient is similar in the measurements of Clark et al. (1966) and Nicovich et al. (1990), and the rate coefficient of the direct reaction is equal to k₆₂ = 4 × 10⁻³³(300/T)^{3.8} cm⁶ s⁻¹ for M = CO₂ with a reasonable confidence.

The equilibrium constant for this species is a ratio of rate coefficients of the direct and reverse processes. Using the data from Nicovich et al. (1990) with their one-sigma errors, this constant is k₆₂/k₆₃ = (2.6 ± 1.1) × 10⁻²⁵ e^{(3770±90)/T} cm³. (This constant is 3.5 × 10⁻²⁵ e^{3730/T} cm³ in Sander et al. (2011) with a reference to Nicovich et al. (1990).) Yung and DeMore (1982) applied the constant of 2.2 × 10⁻²⁴ e^{3250/T} cm³ from the measurements of Burns and Dainton (1952). These constants are equal to (4.0 and 2.5) × 10⁻¹⁷ cm³ at 200 K and (0.75 and 1.1) × 10⁻¹⁹ cm³ at 300 K, that is, the difference between the constants is of a factor of 1.5. An uncertainty of the equilibrium constant was given in Sander et al. (2002) as a factor of 5e^{500(1/T-1/300)}}, that is, near a factor of 10, and was significantly overestimated. This uncertainty was reduced in Sander et al. (2011) to 1.2e^{200(1/T-1/300)}} ≈ 1.5, in accord with our consideration.

Variations of the equilibrium constant up to two standard deviations assessed by Sander et al. (2002), that is, its increase by up to two orders of magnitude, was studied by Mills (1998) and Mills and Allen (2007) to improve fitting of their models to the upper limit of 8 × 10¹⁷ cm⁻² to the O₂ column abundance above 65 km (Trauger and Lunine, 1983; Krasnopolsky, 2006b). Zhang et al. (2012) adopted the equilibrium constant exceeding that of Nicovich et al. (1990) by a factor of 40. There is no clear basis for variations of the equilibrium constant, and we will use the value from Nicovich et al. (1990) and will not vary it in our model.

2.8. Reactions, boundary conditions, and method of solution

Our model involves 153 reactions (Tables 4 and 5) of 44 species (Table 3). This number is much smaller than 381 reactions of 48

Table 5
Reactions, their rate coefficients, column rates, and mean altitudes.

#	Reaction	Rate coefficient ^a	Reference	Column rate ^b	h (km)
31	$O^+ + CO_2 \rightarrow O + CO_2$	$7.5 \times 10^{-11} e^{115/T}$	Sander et al. (2011)	1.58 + 12	82
32	$O^+ + H_2O \rightarrow OH + OH$	$1.6 \times 10^{-10} e^{60/T}$	Sander et al. (2011)	3.49 + 6	79
33	$O^+ + HCl \rightarrow OH + Cl$	1.5×10^{-10}	Sander et al. (2011)	6.23 + 5	81
34	$O_2^+ \rightarrow O_2 + hv$	2.2×10^{-4}	Lafferty et al. (1998)	8.48 + 11	92
35	$O_2^+ + CO_2 \rightarrow O_2 + CO_2$	10^{-20}	Krasnopolsky (2010a)	1.16 + 12	78
36	$O + CO + M \rightarrow CO_2 + M$	$2.2 \times 10^{-33} e^{-1780/T}$	Inn (1974)	4.77 + 10	68
37	$O + O + M \rightarrow O_2 + M^c$	$7.5 \times 10^{-33} (300/T)^{3.25}$	Smith and Robertson (2008) ^d	6.98 + 11	94
38	$O + O_2 + M \rightarrow O_3 + M$	$1.2 \times 10^{-27} T^{-2.4}$	Sander et al. (2011) ^d	8.53 + 12	76
39	$O + O_3 \rightarrow O_2 + O_2$	$8 \times 10^{-12} e^{-2060/T}$	Sander et al. (2011)	2.02 + 8	82
40	$H + O_2 + M \rightarrow HO_2 + M$	$10^{-31} (300/T)^{1.3}$	Sander et al. (2011) ^d	3.54 + 11	83
41	$H + O_3 \rightarrow OH + O_2$	$1.4 \times 10^{-10} e^{-470/T}$	Sander et al. (2011)	1.04 + 11	92
42	$O + HO_2 \rightarrow OH + O_2$	$3 \times 10^{-11} e^{200/T}$	Sander et al. (2011)	2.33 + 11	89
43	$O + OH \rightarrow O_2 + H$	$1.1 \times 10^{-10} T^{-0.32} e^{177/T}$	Robertson and Smith (2006)	2.66 + 11	91
44	$CO + OH \rightarrow CO_2 + H$	$2.8 \times 10^{-13} e^{-176/T}$	Frost et al. (1993)	1.20 + 11	77
45	$H + HO_2 \rightarrow OH + OH$	7.2×10^{-11}	Sander et al. (2011)	9.82 + 8	90
46	$H + HO_2 \rightarrow H_2 + O_2$	6.9×10^{-12}	Sander et al. (2011)	9.43 + 7	90
47	$H + HO_2 \rightarrow H_2O + O$	1.6×10^{-12}	Sander et al. (2011)	2.16 + 7	90
48	$OH + HO_2 \rightarrow H_2O + O_2$	$4.8 \times 10^{-11} e^{250/T}$	Sander et al. (2011)	6.92 + 6	87
49	$OH + O_3 \rightarrow HO_2 + O_2$	$1.7 \times 10^{-12} e^{-940/T}$	Sander et al. (2011)	1.57 + 5	83
50	$H + HCl \rightarrow H_2 + Cl$	$6.6 \times 10^{-16} T^{1.44} e^{-1240/T}$	Adusei and Fontijn (1994)	2.31 + 9	71
51	$OH + HCl \rightarrow H_2O + Cl$	$1.7 \times 10^{-12} e^{-230/T}$	Atkinson et al. (2007)	3.16 + 9	71
52	$O + HCl \rightarrow OH + Cl$	$10^{-11} e^{-3300/T}$	Sander et al. (2011)	1.60 + 9	69
53	$Cl + H_2 \rightarrow HCl + H$	$3.9 \times 10^{-11} e^{-2310/T}$	Atkinson et al. (2007)	2.40 + 9	71
54	$Cl + HO_2 \rightarrow HCl + O_2$	$1.8 \times 10^{-11} e^{170/T}$	Atkinson et al. (2007)	6.71 + 10	75
55	$Cl + HO_2 \rightarrow OH + ClO$	$6.3 \times 10^{-11} e^{-570/T}$	Atkinson et al. (2007)	7.58 + 9	74
56	$OH + ClO \rightarrow HCl + O_2$	$10^{-13} e^{600/T}$	Bedjanian et al. (2001)	1.16 + 6	81
57	$OH + ClO \rightarrow HO_2 + Cl$	1.9×10^{-11}	Atkinson et al. (2007)	1.07 + 7	79
58	$H + Cl_2 \rightarrow HCl + Cl$	$8 \times 10^{-11} e^{-416/T}$	Berho et al. (1999)	2.49 + 10	72
59	$Cl + Cl + M \rightarrow Cl_2 + M$	$5 \times 10^{-26} T^{-2.4}$	Weng et al. (1987), Widman and DeGraff (1973)	1.64 + 13	72
60	$Cl + O_3 \rightarrow ClO + O_2$	$2.8 \times 10^{-11} e^{-250/T}$	Atkinson et al. (2007)	6.89 + 12	74
61	$ClO + O \rightarrow Cl + O_2$	$2.5 \times 10^{-11} e^{110/T}$	Atkinson et al. (2007)	3.50 + 12	77
62	$Cl + CO + M \rightarrow ClCO + M$	$4 \times 10^{-33} (300/T)^{3.8}$	Nicovich et al. (1990) ^{d,e}	5.14 + 15/4.12 + 12	71
63	$ClCO + M \rightarrow Cl + CO + M$	$1.2 \times 10^{-9} e^{-2960/T}$	Nicovich et al. (1990) ^d	5.14 + 15	71
64	$ClCO + Cl \rightarrow CO + Cl_2$	$1.1 \times 10^{-10} e^{-706/T}$	Clark et al. (1966)	2.33 + 11	74
65	$ClCO + NO_2 \rightarrow CO_2 + NO + Cl$	$6 \times 10^{-13} e^{600/T}$	Thomas and Woodman (1967)	2.80 + 9	72
66	$ClCO + ClNO \rightarrow COCl_2 + NO$	$8 \times 10^{-11} e^{-573/T}$	Burns and Dainton (1952)	1.49 + 8	70
67	$ClCO + Cl_2 \rightarrow COCl_2 + Cl$	$4.2 \times 10^{-12} e^{-1490/T}$	Burns and Dainton (1952)	2.05 + 8	71
68	$ClCO + O \rightarrow CO_2 + Cl$	3×10^{-11}	Yung and DeMore (1982)	4.23 + 11	85
69	$ClCO + S \rightarrow OCS + Cl$	3×10^{-11}	Assumed	2.04 + 7	74
70	$ClCO + O_2 + M \rightarrow ClCO_3 + M$	$5.7 \times 10^{-32} e^{500/T} / (1 + M/2 \times 10^{18})$	Yung and DeMore (1982)	3.49 + 12	74
71	$ClCO_3 + Cl \rightarrow CO_2 + Cl + ClO$	10^{-11}	Yung and DeMore (1982)	3.10 + 12	74
72	$ClCO_3 + O \rightarrow CO_2 + Cl + O_2$	10^{-11}	Yung and DeMore (1982)	2.68 + 11	77
73	$ClCO_3 + H \rightarrow CO_2 + Cl + OH$	10^{-11}	Yung and DeMore (1982)	1.31 + 8	82
74	$COCl_2 + O \rightarrow ClCO + ClO$	10^{-14}	Herron (1988)	7.13 + 7	71
75	$N + O \rightarrow NO + hv$	$3.3 \times 10^{-16} T^{-0.5}$	Dalgarno et al. (1992)	7.53 + 7	99
76	$N + O + M \rightarrow NO + M$	$3.5 \times 10^{-31} T^{-0.5}$	Campbell and Thrush (1966)	1.88 + 8	94
77	$N + NO \rightarrow N_2 + O$	$2.2 \times 10^{-11} e^{160/T}$	Wennberg et al. (1994)	3.56 + 8	93
78	$NO + O + M \rightarrow NO_2 + M$	$10^{-27} T^{-1.5}$	Sander et al. (2011) ^d	1.17 + 12	68
79	$NO + O_3 \rightarrow NO_2 + O_2$	$3 \times 10^{-12} e^{-1500/T}$	Sander et al. (2011)	6.53 + 9	66
80	$NO + HO_2 \rightarrow NO_2 + OH$	$3.5 \times 10^{-12} e^{250/T}$	Sander et al. (2011)	7.82 + 10	65
81	$NO_2 + O \rightarrow NO + O_2$	$5.1 \times 10^{-12} e^{210/T}$	Sander et al. (2011)	1.36 + 12	71
82	$NO_2 + O + M \rightarrow NO_3 + M$	$0.7 \times 10^{-26} T^{-1.8}$	Sander et al. (2011) ^d	1.20 + 11	69
83	$NO_3 + NO \rightarrow 2 NO_2$	$1.5 \times 10^{-11} e^{170/T}$	Sander et al. (2011)	5.82 + 10	68
84	$NO_3 + O \rightarrow NO_2 + O_2$	10^{-11}	Sander et al. (2011)	2.51 + 10	70
85	$N + O_2 \rightarrow NO + O$	$2 \times 10^{-18} T^{2.15} e^{-2560/T}$	Fernandez et al. (1998)	6.26 + 5	92
86	$NO + Cl + M \rightarrow ClNO + M$	$2 \times 10^{-31} (300/T)^{1.8}$	Sander et al. (2011) ^d	1.02 + 13	70
87	$ClNO + Cl \rightarrow Cl_2 + NO$	$5.8 \times 10^{-11} e^{100/T}$	Sander et al. (2011)	1.00 + 13	71
88	$ClNO + O \rightarrow NO + ClO$	$8.3 \times 10^{-12} e^{-1520/T}$	Abbatt et al. (1989)	1.54 + 8	68
89	$NO + ClO \rightarrow NO_2 + Cl$	$6.2 \times 10^{-12} e^{295/T}$	Atkinson et al. (2007)	4.22 + 12	71
90	$NO + ClO_2 \rightarrow ClNO + O_2$	4.5×10^{-11}	Enami et al. (2006)	3.19 + 8	73
91	$NO_2 + SCl \rightarrow NO + OSCl$	2.3×10^{-11}	Murrells (1988b)	8.96 + 8	70
92	$SO_2 + O + M \rightarrow SO_3 + M$	$5 \times 10^{-22} T^{-3} e^{-2400/T}$	Naidoo et al. (2005) ^d	5.10 + 11	66
93	$SO_2 + OH + M \rightarrow HSO_3 + M$	$3.5 \times 10^{-20} T^{-4.3}$	Sander et al. (2011) ^d	4.84 + 10	65
94	$SO_2 + Cl + M \rightarrow ClSO_2 + M$	$1.3 \times 10^{-34} e^{940/T}$	Mills (1998)	8.01 + 12	69
95	$ClSO_2 + H \rightarrow SO_2 + HCl$	10^{-11}	Krasnopolsky (2007)	3.55 + 9	67
96	$ClSO_2 + Cl \rightarrow SO_2 + Cl_2$	10^{-12}	Krasnopolsky (2007)	5.14 + 12	70
97	$ClSO_2 + O \rightarrow SO_2 + ClO$	10^{-12}	Assumed	5.56 + 11	69
98	$ClSO_2 + SCl \rightarrow SO_2 + SCl_2$	10^{-13}	Assumed	2.32 + 7	69
99	$HSO_3 + O_2 \rightarrow SO_3 + HO_2$	$1.3 \times 10^{-12} e^{-330/T}$	Sander et al. (2011)	4.84 + 10	65
100	$S + O_2 \rightarrow SO + O$	2.3×10^{-12}	Sander et al. (2011)	2.45 + 12	72
101	$S + O_3 \rightarrow SO + O_2$	1.2×10^{-11}	Sander et al. (2011)	1.04 + 9	69
102	$S + NO + M \rightarrow SNO + M$	$3 \times 10^{-32} e^{940/T}$	Goumri et al. (2004)	1.09 + 11	59
103	$SNO + O \rightarrow NO + SO$	10^{-11}	Assumed	2.68 + 9	67
104	$SO + O + M \rightarrow SO_2 + M$	$1.3 \times 10^{-30} (300/T)^{2.2}$	Lu et al. (2003) ^d	2.70 + 12	73

(continued on next page)

Table 5 (continued)

#	Reaction	Rate coefficient ^a	Reference	Column rate ^b	h (km)
105	SO + O ₂ → SO ₂ + O	1.25 × 10 ⁻¹³ e ^{-2190/T}	Sander et al. (2011)	3.95 + 10	73
106	SO + O ₃ → SO ₂ + O ₂	3.4 × 10 ⁻¹² e ^{-1100/T}	Sander et al. (2011)	5.01 + 9	69
107	SO + OH → SO ₂ + H	2.7 × 10 ⁻¹¹ e ^{335/T}	Sander et al. (2011)	6.63 + 9	86
108	SO + ClO → SO ₂ + Cl	2.8 × 10 ⁻¹¹	Sander et al. (2011)	2.86 + 12	74
109	SO + ClO ₂ → SO ₂ + ClO	1.9 × 10 ⁻¹²	Sander et al. (2011)	1.43 + 7	77
110	SO + HO ₂ → SO ₂ + OH	2.8 × 10 ⁻¹¹	Yung and DeMore (1982)	1.54 + 10	70
111	SO + SO → SO ₂ + S	3.5 × 10 ⁻¹⁵	Martinez and Herron (1983)	8.05 + 9	74
112	SO + NO ₂ → SO ₂ + NO	1.4 × 10 ⁻¹¹	Sander et al. (2011)	2.68 + 12	70
113	SO + SO ₃ → SO ₂ + SO ₂	2 × 10 ⁻¹⁵	Chung et al. (1975)	9.44 + 8	69
114	SO ₃ + O → SO ₂ + O ₂	2.3 × 10 ⁻¹⁶ e ^{-487/T}	Jacob and Winkler (1972)	6.88 + 6	69
115	SO ₃ + H ₂ O + H ₂ O → H ₂ SO ₄ + H ₂ O	2.3 × 10 ⁻⁴³ T e ^{6540/T}	Loverjoy et al. (1996)	5.71 + 11	66
116	Cl + O ₂ + M → ClO ₂ + M	5 × 10 ⁻³³ (300/T) ^{3.1}	Sander et al. (2011) ^{d,e}	4.73 + 14/1.54 + 10	73
117	ClO ₂ + M → Cl + O ₂ + M	7 × 10 ⁻¹⁰ e ^{-1820/T}	Sander et al. (2011)	4.73 + 14	73
118	O + Cl ₂ → ClO + Cl	7.4 × 10 ⁻¹² e ^{-1650/T}	Wine et al. (1985)	4.69 + 10	71
119	Cl + O + M → ClO + M	5 × 10 ⁻³²	Yung and DeMore (1982)	4.02 + 11	73
120	S + S + M → S ₂ + M	10 ⁻³² e ^{206/T}	Du et al. (2008) ^d	2.72 + 4	62
121	S + S ₂ + M → S ₃ + M	10 ⁻³² e ^{206/T}	k ₁₂₀	9.76 + 5	58
122	S ₂ + S ₂ + M → 4 S ₃ + M	10 ⁻³² e ^{206/T}	k ₁₂₀	1.62 + 8	56
123	S + S ₃ → S ₂ + S ₂	1.7 × 10 ⁻¹⁰ e ^{-2800/T}	Krasnopolsky (2007)	0.02	59
124	S ₂ + S ₃ + M → 5S ₄ + M	10 ⁻³² e ^{206/T}	k ₁₂₀	99	58
125	O + S ₂ → SO + S	2.2 × 10 ⁻¹¹ e ^{-84/T}	Craven and Murrell (1987)	3.47 + 6	61
126	O + S ₃ → SO + S ₂	5 × 10 ⁻¹¹	Assumed	14	60
127	O + S ₃ → SO	γ = 0.01	Assumed	8.41 + 7	70
128	SO + SO + M → S ₂ O ₂ + M	10 ⁻³⁰	Herron and Huie (1980) ^d	1.84 + 12	70
129	S ₂ O ₂ + O → S ₂ O + O ₂	3 × 10 ⁻¹⁴	Yung and DeMore (1982)	3.64 + 9	71
130	S ₂ O ₂ + O → SO ₂ + SO	3 × 10 ⁻¹⁵	Yung and DeMore (1982)	3.64 + 8	71
131	S ₂ O ₂ + SO → S ₂ O + SO ₂	3.3 × 10 ⁻¹⁴	Herron and Huie (1980)	6.98 + 9	70
132	S ₂ O + O → SO + SO	1.5 × 10 ⁻¹²	Singleton and Cvetanovic (1988)	3.32 + 8	70
133	S ₂ O + Cl → SCl + SO	10 ⁻¹²	Assumed	2.31 + 9	71
134	ClCO ₃ + SO → Cl + SO ₂ + CO ₂	10 ⁻¹²	Assumed	3.08 + 10	74
135	ClCO ₃ + SO ₂ → Cl + SO ₃ + CO ₂	10 ⁻¹⁴	Assumed	1.83 + 10	69
136	O + OCS → SO + CO	1.6 × 10 ⁻¹¹ e ^{-2150/T}	Atkinson et al. (2007)	4.24 + 8	65
137	S + OCS → S ₂ + CO	2.4 × 10 ⁻²⁴ T ⁴ e ^{-580/T}	Lu et al. (2006)	3.75 + 8	57
138	S + CO + M → OCS + M	3 × 10 ⁻³³ e ^{-1000/T}	Krasnopolsky (2007)	5.02 + 10	58
139	S + Cl ₂ → SCl + Cl	2.8 × 10 ⁻¹¹ e ^{-290/T}	Baulch et al. (1981)	2.84 + 10	70
140	O + SCl → SO + Cl	1.2 × 10 ⁻¹⁰	Murrells (1988b)	1.95 + 10	70
141	Cl + SCl + M → SCl ₂ + M	10 ⁻³⁰	Mills (1998)	2.74 + 9	70
142	Cl ₂ + SCl → SCl ₂ + Cl	7 × 10 ⁻¹⁴	Murrells (1988a)	2.78 + 8	70
143	ClO ₂ + O → ClO + O ₂	2.4 × 10 ⁻¹² e ^{-960/T}	Atkinson et al. (2007)	3.43 + 5	84
144	ClO ₂ + Cl → Cl ₂ + O ₂	10 ⁻¹⁰	Sander et al. (2011)	7.51 + 9	76
145	ClO ₂ + Cl → ClO + ClO	10 ⁻¹⁰	Assumed	7.51 + 9	76
146	SO + Cl + M → OSCL + M	5 × 10 ⁻³³ (300/T) ^{3.1}	k ₁₁₆	1.61 + 11	72
147	OSCL + O → SO ₂ + Cl	10 ⁻¹²	Assumed	1.08 + 10	72
148	OSCL + Cl → SO + Cl ₂	10 ⁻¹²	Assumed	1.52 + 11	72
149	ClSO ₂ + ClSO ₂ → SO ₂ Cl ₂ + SO ₂	10 ⁻¹²	Krasnopolsky (2007)	2.31 + 12	66
150	ClSO ₂ + SCl → SO ₂ Cl ₂ + S	10 ⁻¹³	Assumed	2.32 + 7	69
151	NO ₂ + HO ₂ + M → HO ₂ NO ₂ + M	5 × 10 ⁻³¹ (300/T) ^{3.1}	Christensen et al. (2004) ^d	2.04 + 8	66
152	HO ₂ NO ₂ + M → HO ₂ + NO ₂ + M	10 ⁻⁴ e ^{-10600/T}	Zabel (1995) ^d	1.88 + 7	65
153	HO ₂ NO ₂ + OH → NO ₂ + O ₂ + H ₂ O	1.3 × 10 ⁻¹² e ^{380/T}	Sander et al. (2011)	1.01 + 5	66

^a In cm³ s⁻¹ and cm⁶ s⁻¹ for two- and three-body reactions, respectively. Aerosol uptake coefficients are dimensionless.

^b For the basic model, in cm⁻² s⁻¹, see text.

^c Yield of O₂(¹Δ_g) is 0.7.

^d Corrected for the higher efficiency of CO₂ than N₂ and Ar as a third-body by factors of 2.5 and 5, respectively.

^e Difference between the direct and inverse reactions is also given.

species in Mills (1998) and 341 reactions in Zhang et al. (2012). We have greatly reduced the number of S_X reactions (section 2.6) and use M = CO₂ for all termolecular reactions. (Reactions for a few M are considered in Zhang et al. (2012); for example, O + O₂ + M → O₃ + M is given for M = CO₂, N₂, CO, O₂, and O, though the total effect of N₂, CO, O₂, and O is ~1% of that of CO₂ and well within its uncertainty.) Our approach reflects the intention to remove unimportant species and reactions. Actually a further reduction could be made using the calculated model; however, we have not done this.

Nitrogen chemistry in our model is based on that in models of the middle and lower atmosphere of Mars (Nair et al., 1994; Krasnopolsky, 1995). Nitrogen acids HNO_X are expected to be even scarcer than in the martian models. Therefore, only the most abundant acid HO₂NO₂ is present in our model.

The model includes species of six elements (O, C, N, S, Cl, and H), and six corresponding source species are constrained by their den-

sities at the lower boundary (Krasnopolsky, 1995). However, the H₂ mixing ratio in the lower atmosphere is controlled by equilibria in the reactions HCl + H ↔ H₂ + Cl and H₂S + H ↔ H₂ + SH (Krasnopolsky, 2007) and does not depend on processes in the middle atmosphere. Therefore, the H₂ mixing ratio of 4.5 ppb is among the lower boundary conditions in Table 6. The boundary conditions for HCl (Krasnopolsky, 2010b and references therein) and NO (Krasnopolsky, 2006a) are from the observations, and those for H₂O, OCS, and H₂ are from the kinetic model (Krasnopolsky, 2007). The condition for SO₂ is a fitting parameter, and the value in Table 6 is for our basic model.

The conditions for the other species are velocities V. V = 0 corresponds to a constant mixing ratio at the boundary, V = -K/H corresponds to a constant number density, and we assume V = -K/2H as the mean. According to our model, a constant number density is the case for O₂, and V = -K/H is applied to this species. The value for CO will be discussed below.

Table 6

Conditions at the lower boundary (47 km).

CO ₂	H ₂ O	SO ₂	HCl	OCS	NO	H ₂	CO	O ₂	Other
$3.6 \times 10^{19} \text{ cm}^{-3}$	21 ppm	9.7 ppm	400 ppb	260 ppb	5.5 ppb	4.5 ppb	0.1 V	2 V	V

$$V = -K/2H = -0.006 \text{ cm s}^{-1}.$$

Table 7

Fluxes at the upper boundary (112 km).

CO	O ₂	O	N	Other
-6×10^{11}	[O ₂] V	$-6 \times 10^{11} - 2[\text{O}_2] V$	-6×10^8	0

Fluxes are in $\text{cm}^{-2} \text{ s}^{-1}$, $V = (J_4 + J_5)H = 0.3 \text{ cm s}^{-1}$.

Conditions at the upper boundary are fluxes for CO, O₂, O, and N (Table 7). The flux of CO in the global-mean model is just half the number of the solar photons absorbed above 112 km for the solar zenith angle of 60°. The condition for O₂ is actually velocity that is equal to the O₂ photolysis frequency at 112 km times the scale height. The flux of O is a sum of the CO₂ and O₂ photolyses above 112 km.

The flux of N is more uncertain. The Venus Express observations of the O₂ and NO nightglow (Piccioni et al., 2009; Gerard et al., 2008) and the model of the nighttime photochemistry (Krasnopolsky, 2010a) indicate effective transport of O and N to the night side, where the observed fluxes approach the global-mean values. The observed nightside mean NO nightglow intensity of 400 R requires a flux of N of $1.2 \times 10^9 \text{ cm}^{-2} \text{ s}^{-1}$ (Krasnopolsky, 2010a). Half of this flux is lost above 112 km, and the adopted flux is $6 \times 10^8 \text{ cm}^{-2} \text{ s}^{-1}$ in our model.

Fluxes of all other species are low and assumed equal to zero. The model results are not very sensitive to the fluxes at the upper boundary.

A one-dimensional steady-state photochemical problem for a spherical atmosphere is a set of the continuity equations for each species with the vertical transport by eddy diffusion and sources and sinks in chemical reactions. These continuity equations are

the ordinary second-order nonlinear differential equations. A set of 44 finite difference analogs to these equations is solved using a method described in Krasnopolsky and Cruikshank (1999).

3. Results of the model

The calculated column reaction rates per cm^2 , CR, and mean altitudes h_m for all reactions are given in Tables 4 and 5. The values are corrected for sphericity:

$$CR = \int_{47.5 \text{ km}}^{111.5 \text{ km}} r(h)(1+h/R_0)^2 dh;$$

$$h_m = \frac{1}{CR} \int_{47.5 \text{ km}}^{111.5 \text{ km}} r(h)(1+h/R_0)^2 h dh$$

though this correction is small for Venus. Here $r(h)$ is the reaction rate and $R_0 = 6052 \text{ km}$ is the Venus surface radius. Chemical reactions at the boundaries are not involved in chemical balances in the finite difference schemes for photochemical models, and the integration limits reflect this fact. Column rates and mean altitudes of reactions are convenient tools to study species balances and as quantitative evaluations of chemical processes. Although the column rates and the mean altitudes do not cover all information on the model, models without these data are difficult to analyze by the readers.

3.1. Carbon monoxide

Photolysis of CO₂ (Fig. 2) forms CO with a column rate of $4.7 \times 10^{12} \text{ cm}^{-2} \text{ s}^{-1}$ including the flux from the upper atmosphere.

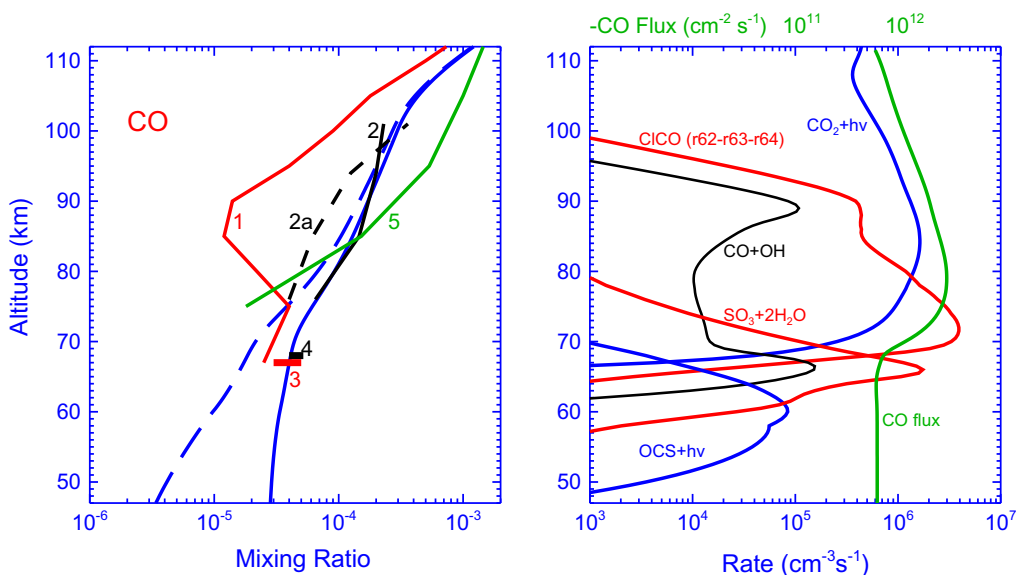
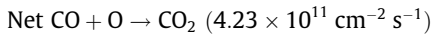
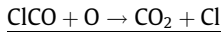
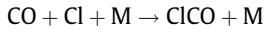


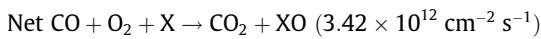
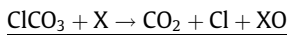
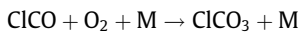
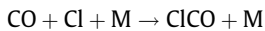
Fig. 2. Left panel: calculated profiles of the CO mixing ratio for $V = -K/2H$ and $-K/20H$ at 47 km (dashed and solid blue lines, respectively). CO observations: (1) VEX/SOIR (Vandaele et al., 2008); (2) Clancy et al. (2012), dayside observations in 2001–2002; (2a) Clancy et al. (2012), dayside observations in 2007–2009; (3) VEX/VIRTIS (Irwin et al., 2008); (4) Connes et al. (1968) and Krasnopolsky (2010b); (5) Lellouch et al. (1994). Right panel: main reactions of production and loss of CO. The CICO cycle is shown as difference r62–r63–r64. Production of sulfuric acid is shown as well. (For interpretation of the references to color in this figure legend, the reader is referred to the web version of this article.)

The small increase in the photolysis above 108 km is due to the solar Lyman-alpha emission, which is mostly absorbed above 112 km. Photolysis of OCS (Fig. 2) is another source of CO that is weaker by two orders of magnitude.

The CICO cycles are the main processes of recombination of CO₂ and loss of CO:



and



where X = Cl, O, SO, SO₂, and H. Photolysis of CICO₃ ($7.9 \times 10^{10} \text{ cm}^{-2} \text{ s}^{-1}$) has a similar effect. The CO loss in the cycles, $3.9 \times 10^{12} \text{ cm}^{-2} \text{ s}^{-1}$, is much greater than those in the odd hydrogen cycle and termolecular reactions with O and S (1.2×10^{11} , 4.8×10^{10} , and $5.0 \times 10^{10} \text{ cm}^{-2} \text{ s}^{-1}$, respectively). The difference between the production and loss leads to a net downward flux of CO in the lower atmosphere that appears equal to that from the upper atmosphere.

The calculated CO profile for the standard boundary condition $V = -K/2H$ is shown by the dashed line in Fig. 2. The CO mixing ratio at the cloud tops (68 km) is 19 ppm, smaller than that measured by VIRTIS (Irwin et al., 2008) and ground-based spectroscopy (Connes et al., 1968; Krasnopolsky, 2010b) by a factor of ~2.

The CO density at the lower boundary was fixed at 45 ppm in Mills (1998) and Zhang et al. (2012). Mills and Allen (2007) adopted $V = -K/H$ for CO at 58 km and calculated 6 ppm of CO at 68 km. We have reduced V for CO by a factor of 10 in our standard model to better fit the observations. The CO mixing ratio near the cloud tops varies within a factor of 2 (Table 8) when the eddy breakpoint h_e changes from 55 to 65 km (Fig. 1).

Vertical profiles of the CO mixing ratio were measured in the submillimeter range (Lellouch et al., 1994; Clancy et al., 2012) and by VEX/SOIR (Vandaele et al., 2008). Mean profiles from these measurements are shown in Fig. 2. Our model is good agreement with the observations, especially with Clancy et al. (2012). The calculated CO mixing ratio is 10^{-3} at 112 km, similar to that in Mills (1998) and the mean measured values in Lellouch et al. (1994) and Vandaele et al. (2008) and smaller than 4×10^{-3} in Zhang et al. (2012).

3.2. Sulfur species

Sulfur drives the chemistry in the lower atmosphere (Krasnopolsky, 2007) and is essential in the middle atmosphere, where the sulfuric acid aerosol and gaseous SO₂, SO, and OCS are measured by various spacecraft and ground-based instruments. Photolysis of SO₂ exceeds that of CO₂ by a factor of 2.5 (Table 4) initiating intense sulfur chemistry. The observed high variability of SO₂, SO, and OCS is of special interest and needs to be explained in terms of photochemistry and atmospheric dynamics. Furthermore, sulfur species are abundant in the volcanic gases, and the volcanic activity may be considered among possible sources of the observed variations of sulfur species (Esposito et al., 1988).

We find that the abundances of sulfur species are very sensitive to small variations of eddy diffusion and the adopted SO₂ mixing ratio at the lower boundary. These facts were established by Krasnopolsky and Parshev (1981, 1983), and here we confirm their conclusion. We choose SO₂ = 9.7 ppm at 47 km and the eddy breakpoint $h_e = 60$ km in our standard model. The calculated vertical profiles of SO₂, SO, OCS, and aerosol sulfur S_a are shown in Fig. 3. Mills (1998), Mills and Allen (2007), and Zhang et al. (2012) adopted SO₂ = 1, 1, and 3.5 ppm, respectively, at their lower boundary of 58 km. Our model gives 6 ppm at this height.

Sulfuric acid mostly forms in (R92) SO₂ + O + M followed by (R115) SO₃ + H₂O + H₂O with a column rate of $5.7 \times 10^{11} \text{ cm}^{-2} \text{ s}^{-1}$. This rate is similar to those calculated by Mills (1998) and Mills and Allen (2007), 6×10^{11} and $4.8 \times 10^{11} \text{ cm}^{-2} \text{ s}^{-1}$, respectively, though they did not include photolysis of SO₃; this rate is $5.6 \times 10^{11} \text{ cm}^{-2} \text{ s}^{-1}$ in Zhang et al. (2012). The sulfuric acid mean yield relative to the SO₂ photolysis is 0.056. Sulfuric acid is formed in a narrow layer with a peak at 66 km and a width of 3 km at half maximum (Fig. 2). This layer is at the bottom of the SO₂ photolysis where M and H₂O are large, (R92) and (R115) are effective, and the yield is close to one.

The formation of sulfuric acid greatly reduces the SO₂ mixing ratio to ~100 ppb near 70 km (Fig. 3). SO produced by the SO₂ photolysis above ~70 km regenerates SO₂, mostly in the reactions with ClO, NO₂ and (R104) SO + O + M. The close balance between SO₂ photolysis and regeneration at 75–95 km and the increasing eddy diffusion tends to keep a constant SO₂ mixing ratio of ~30 ppb at these altitudes where [SO] < [SO₂]. The regeneration reactions become ineffective above 100 km, and SO₂ decreases above this height because of its photolysis.

SO is the main photochemical product of SO₂ above 75 km, where the formation of sulfuric acid is ineffective. (R112) SO + NO₂ is mostly responsible for the removal of SO below 75 km. A sum of the SO₂ and SO mixing ratios is nearly constant above 80 km, SO₂/SO ≈ 3 at 80–95 km, and SO dominates above 100 km.

The OCS mixing ratio of 260 ppb at 47 km from the kinetic model by Krasnopolsky (2007) is the lower boundary condition in our model. Photolysis of OCS is strongly affected by absorption by

Table 8

Variations of the observable species in the model induced by variations of the eddy breakpoint h_e , SO₂ at 47 km, and V_{CO} at 47 km.

h_e	SO ₂ 47 km	V_{CO} 47 km	CO 68 km	O ₂ 65 km	H ₂ O 75 km	SO ₂ 70 km	SO ₂ 90 km	SO 90 km	OCS 65 km
60 km	9.7 ppm	$-K/20H$	41.2 ppm	$7.66 + 18 \text{ cm}^{-2}$	1.18 ppm	85 ppb	28.3 ppb	8.0 ppb	2.7 ppb
55	9.7	$-K/20H$	66.3	$7.58 + 18$	1.68	638	197	41	3.5
65	9.7	$-K/20H$	31.3	$1.15 + 19$	1.15	33	5.7	2.1	184
60	9.7	$-K/2H$	18.5	$9.03 + 18$	1.24	128	44	12.3	0.9
60	9.2	$-K/20H$	41.6	$8.64 + 18$	2.16	76	22.3	6.8	1.5
60	10.2	$-K/20H$	40.6	$6.13 + 18$	0.36	186	95	24.5	2.8

$7.66 + 18 = 7.66 \times 10^{18}$.

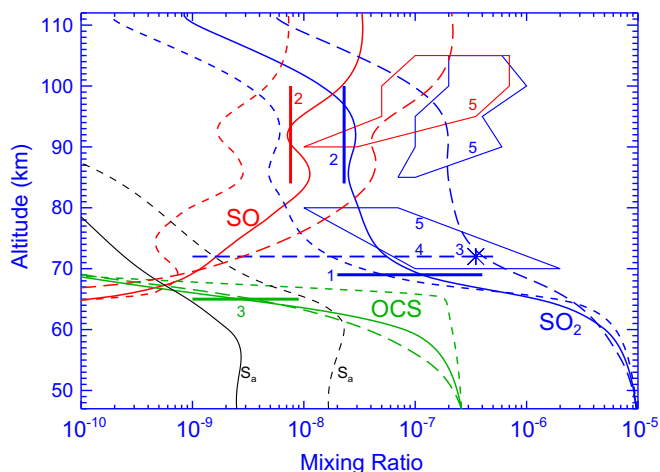


Fig. 3. Basic sulfur species: model results and observations. SO_2 , OCS, and SO profiles are shown for the models with the eddy break at $h_e = 55$, 60, and 65 km (long dash, solid, and short dash curves, respectively). The aerosol sulfur S_a mixing ratio is 4×10^{-11} at 47 km for $h_e = 55$ km and not shown. Observations: (1) PV, Venera 15, HST and rocket data (Esposito et al., 1997); (2) mean results of the submillimeter measurements (Sandor et al., 2010); the observed SO_2 varies from 0 to 76 ppb and SO from 0 to 31 ppb; (3) IRTF/CSHELL (Krasnopolsky, 2010c); (4) SPICAV-UV, nadir (Marcq et al., 2011); (5) VEX/SOIR and SPICAV-UV occultations (Belyaev et al., 2012).

SO_2 and the NUV absorber. OCS is 110 ppb at 58 km, very similar to the adopted boundary condition of 100 ppb in Mills (1998) and Mills and Allen (2007) and much smaller than 1.5 ppm in Zhang et al. (2012). However, the decrease of OCS is steeper in Mills (1998) and Zhang et al. (2012) than that in our model, with $\text{OCS} \approx 0.01$ ppb, 2, and 2 ppb, respectively, at 65 km.

The aerosol sulfur (Fig. 3) is a minor species in the model with a mixing ratio of 2.5 ppb below 60 km. Photolysis of SO was the main source of free sulfur in the previous models. Reactions



are more effective in our model. Atomic sulfur is mostly lost in the reaction with O_2 , which restricts the sulfur aerosol formation.

We have not found data on photodissociation of S_2O_2 in the literature. According to Marsden and Smith (1990), the lowest energy isomer of S_2O_2 has a structure that is similar to SO_3 with one oxygen atom replaced by a sulfur atom, and its binding energy is ~ 1 eV relative to two SO molecules. Then we conclude that $\text{SO}_2 + \text{S}$ is the most probable photolysis branch with a dissociation energy of ~ 0.7 eV. The model is almost insensitive to the S_2O_2 photolysis frequency, which is chosen similar to that of NO_2 .

Effects of minor variations of eddy diffusion on the abundances of the basic sulfur species are shown in Fig. 3. The eddy breakpoint is changed from 60 km in the basic model to 55 and 65 km in the additional versions. Eddy diffusion controls the amount of SO_2 that can be delivered through the bottleneck near 66 km where sulfuric acid forms. SO_2 varies above 70 km within a factor of ~ 30 , and its variations induce variations of SO.

The S atoms from the OCS photolysis react with either CO (in termolecular association of OCS) or O_2 . The former dominates below 60 km; that is why the steep decrease in OCS occurs above 60 km (Fig. 3). The delivery of O_2 by eddy diffusion becomes weaker if the eddy breakpoint is at 65 km, and the balance between the two reactions of S moves to 65 km as well with a steep decrease in OCS above 65 km in this case.

The abundance of the aerosol sulfur is mostly controlled by the delivery of O_2 that depends on h_e , and S_a is very sensitive to the variations of h_e (Fig. 3).

3.3. Comparison to observations of SO_2 , SO, and OCS

Observations of SO_2 by the PV/UVS, V15/FTS, HST and rocket flights were summarized in Esposito et al. (1997), and the observed range of the results is shown in Fig. 3. The data refer to ~ 70 km and are perfectly centered at our basic model. The SOIR vertical profiles (Belyaev et al., 2008, 2012) at 70–80 km depict variations of ~ 0.1 to ~ 2 ppm at 70 km, and the SPICAV nadir observations (Marcq et al., 2011) of SO_2 near 70 km demonstrate even wider range of the variations. The ground-based detection of SO_2 (Krasnopolsky, 2010c) gave the abundance near the middle of the SOIR range. Overall, the SO_2 observations at 69–80 km are in excellent agreement with the model, and even exceptionally low SO_2 abundances in some SPICAV nadir observations may be explained by the variations of eddy diffusion in our model.

According to the submillimeter observations of SO_2 and SO (Sandor et al., 2010), their mixing ratios at 84–100 km vary within an order of magnitude with mean values of 23 and 7.5 ppb, respectively, in excellent agreement with the basic model. However, the data require a significant decrease below 84 km that is not supported by both the SOIR observations and our models. Variations of SO_2 by a few times within a few days present another problem in the submillimeter observations. The instrument observed the full disk of Venus or its large parts; to explain these variations using our model, short-term global-scale variations of eddy diffusion should be involved.

The mean SO abundances from the SPICAV solar occultations (Belyaev et al., 2012) are similar to those in the model for $h_e = 55$ km. The mean SO_2 data in those observations below 95 km also agree with the model for $h_e = 55$ km. However, the difference between the SPICAV occultation measurements above 85 km and the SOIR data below 80 km requires a source of SO_x near 100 km that is not supported by the current data on the Venus atmosphere (Krasnopolsky, 2011b). Furthermore, the interpretation of the SO_2 feature in the SPICAV spectra may be not unique (Krasnopolsky, 2011b).

Our model is in excellent agreement with observations of the recently discovered OCS at the cloud tops (Krasnopolsky, 2010c). The model does not involve parameters that facilitate this agreement.

3.4. Water vapor

Water vapor is fixed at 21 ppm at 47 km from the kinetic model by Krasnopolsky (2007). The H_2O mixing ratio is equal to 30 ppm in the lower atmosphere (Pollack et al., 1993), a mixing ratio of H_2SO_4 vapor is 9 ppm at 47 km in Krasnopolsky (2007); therefore, according to the element conservation (Krasnopolsky, 1986, p. 243), the H_2O mixing ratio at 47 km is the difference between these values. Similar to SO_2 , water vapor is lost in the thin layer near 66 km where sulfuric acid forms, and the H_2O mixing ratio is steeply decreasing to 70 km (Fig. 4). The mixing ratio is almost constant above 70 km with a weak decline because of the photolysis. The H_2O abundance above 70 km is sensitive to changes in eddy diffusion and SO_2 at the lower boundary. The anticorrelation with SO_2 is shown in Fig. 4, where the basic model is compared with those with deviations of SO_2 of 5% at 47 km. The change in SO_2 by 10% induces the change in H_2O above 70 km by a factor of 6.

The calculated H_2O profiles are compared in Fig. 4 with observations from airborne observatories by Fink et al. (1972) and Bjoraker et al. (1992), the Venera 15 FTS results (Ignatiev et al., 1999), VEX/VIRTIS (Cottini et al., 2012), ground-based (Encrenaz et al., 1995;

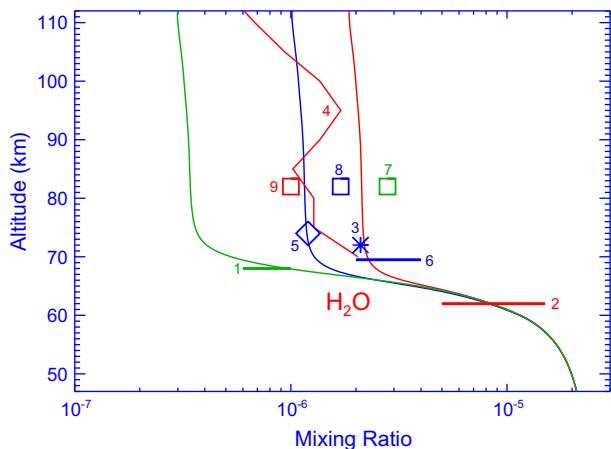


Fig. 4. Profiles of the H_2O mixing ratio: models and observations. Three calculated profiles are for the models with the SO_2 mixing ratio of 10.2 (green), 9.7 (blue), and 9.2 (red) ppm at 47 km. Observations: (1) Fink et al. (1972); (2) Venera 15 (Ignatiev et al., 1999); (3) KAO (Bjoraker et al., 1992); (4) VEX/SOIR (Fedorova et al., 2008); (5) Krasnopolsky (2010c); (6) VEX/VIRTIS (Cottini et al., 2012). Mean results of the microwave observations: (7) Encrenaz et al. (1995); (8) SWAS (Gurwell et al., 2007); (9) Sandor and Clancy (2005). The microwave observations cover the full disk of Venus or its significant parts at altitudes of ~ 70 to 95 km and show high variability of H_2O starting from very low values near zero. The most detailed data by Sandor and Clancy (2005) give 1 ± 1 ppm, where the standard deviation reflects the observed variability of H_2O . (For interpretation of the references to color in this figure legend, the reader is referred to the web version of this article.)

Sandor and Clancy, 2005) and SWAS (Gurwell et al., 2007) microwave measurements, and ground-based NIR observations (Krasnopolsky, 2010c). The Pioneer Venus broadband observations at $45 \mu\text{m}$ showed very large H_2O abundances ~ 90 ppm at low latitudes in the afternoon near 63 km (Koukouli et al., 2005), and these data are not shown in Fig. 4.

Vertical profiles of H_2O were measured by VEX/SOIR (Fedorova et al., 2008), and the mean of their data is shown in Fig. 4. Some of the microwave observations by Sandor and Clancy (2005) resulted in the H_2O mixing ratios in two altitude intervals of 65–82 and 82–100 km; however, no regular altitude dependence has been detected. Their microwave observations were made in 17 sessions in the period of 1998–2004, and the retrieved H_2O mixing ratio at

65–100 km was very variable with a mean value of 1 ± 1 ppm. Overall, the model perfectly agrees with the observations.

3.5. Oxygen allotropes O_x

The calculated vertical profiles of O_2 , O , O_2^+ , and O_3 are shown in Fig. 5, where they are compared with CO_2 and CO . O_2 is involved in many reactions, and main reactions of its formation and loss are shown in the right panel of Fig. 5. Reactions (R61) $\text{O} + \text{ClO}$, (R81) $\text{O} + \text{NO}_2$, (R37) $\text{O} + \text{O} + \text{M}$, and (R43) $\text{O} + \text{OH}$ contribute 60, 23, 12, and 5%, respectively, to the total O_2 production of $5.8 \times 10^{12} \text{ cm}^{-2} \text{ s}^{-1}$. Comparing to the CO_2 and SO_2 photolysis rates, 80% of oxygen atoms released in these photolyses form O_2 . (R37) and (R43) are rather weak but dominate in the production of O_2 above 90 km.

The ClCO cycle and (R100) $\text{S} + \text{O}_2$ are the basic processes of the O_2 loss (57% and 43%, respectively). The effect of the ClCO cycle may be given as a difference between (R70) and (R72):



None of the other losses for ClCO_3 returns O_2 .

The calculated column abundance of O_2 is equal to $7.6 \times 10^{18} \text{ cm}^{-2}$, similar to $8.6 \times 10^{18} \text{ cm}^{-2}$ in the nominal model by Mills and Allen (2007). This abundance exceeds an upper limit of $8 \times 10^{17} \text{ cm}^{-2}$ (Trauger and Lunine, 1983; Krasnopolsky, 2006b) by a factor of 10. To fit the limit, Mills (1998), Mills and Allen (2007), and Zhang et al. (2012) calculated models with the ClCO equilibrium constant increased up to two orders of magnitude (by a factor of 40 in Zhang et al. (2012)). Then the O_2 column becomes $2 \times 10^{18} \text{ cm}^{-2}$, still above the limit. We have discussed in Section 2.5 that a significant increase of the ClCO equilibrium constant is not supported by the laboratory measurements. Furthermore, this increase reduces the CO mixing ratio at the cloud tops to ~ 1.5 ppm (Mills and Allen, 2007), far below the observed value of 40 ppm. Therefore we do not have good ideas how to agree the model O_2 with the observed upper limit.

Although the O_2 column abundances are similar in our model and Mills and Allen (2007), the O_2 profiles are significantly different: constant at $3 \times 10^{12} \text{ cm}^{-3}$ at 58–70 km in Mills and Allen (2007) and variable within three orders of magnitude at these

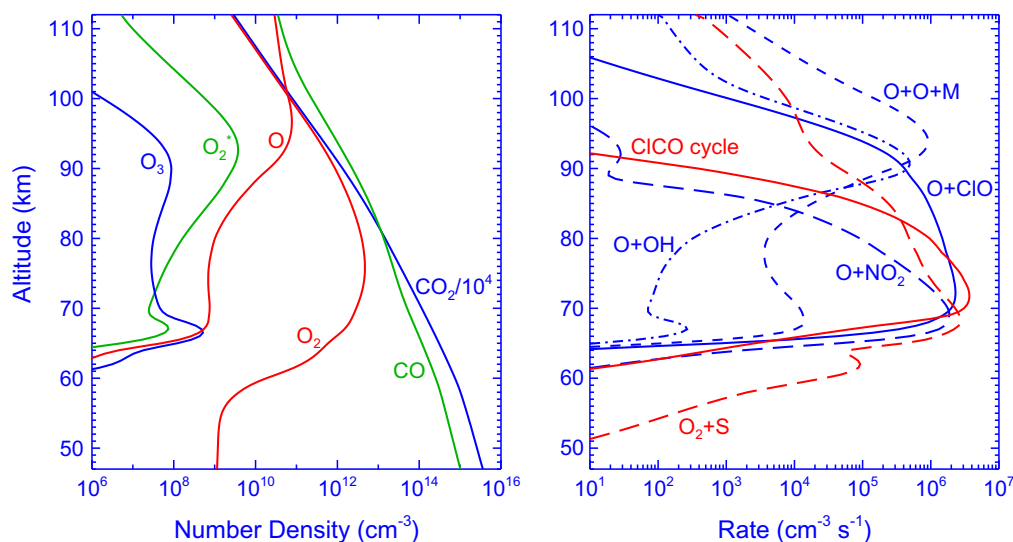


Fig. 5. Left panel: CO_2 and its photochemical products. Right panel: main reactions of formation (blue) and loss (red) of $\text{O}=\text{O}$ bonds. The ClCO cycle is shown as difference between $\text{ClCO} + \text{O}_2 + \text{M} \rightarrow \text{ClCO}_3 + \text{M}$ and $\text{ClCO}_3 + \text{O} \rightarrow \text{CO}_2 + \text{O}_2 + \text{Cl}$. (For interpretation of the references to color in this figure legend, the reader is referred to the web version of this article.)

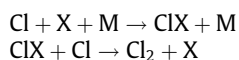
altitudes in our model. This difference is mostly due to the more abundant OCS in our model that forms S by photolysis, and S quickly removes O₂.

The ozone densities are $\sim 4 \times 10^7 \text{ cm}^{-3}$ at 70 to 95 km, smaller than the nighttime values that peak at $3 \times 10^9 \text{ cm}^{-3}$ near 94 km (Krasnopolsky, 2010a).

3.6. Chlorine species and odd hydrogen

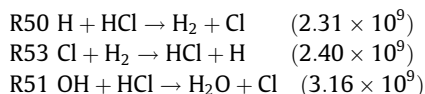
The HCl mixing ratio is nearly constant in our model, slightly decreasing from 400 ppb at the lower boundary to 310 ppb at the upper boundary. Chlorine species in the middle atmosphere of Venus (Figs. 6 and 7) originate from photolysis of HCl that forms equal quantities of H and Cl. Odd hydrogen, that is, H, OH, and HO₂, is also formed by photolysis of H₂O. Its column rate is smaller than that of HCl by a factor of 70. However, the H₂O photolysis exceeds that of HCl above 95 km, and the H densities are greater than Cl above 95 km.

Molecular chlorine is formed in termolecular association $\text{Cl} + \text{Cl} + \text{M}$ and via



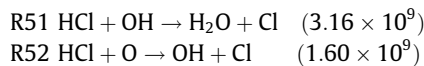
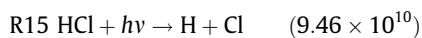
Here X = NO, SO₂, O, CO, SO, and O₂, in the decreasing order, and Cl₂ immediately dissociates with a column rate of $3.18 \times 10^{13} \text{ cm}^{-2} \text{ s}^{-1}$ that significantly exceeds the rates of the CO₂ and SO₂ photolyses.

A balance between odd hydrogen and chlorine species is established via reactions



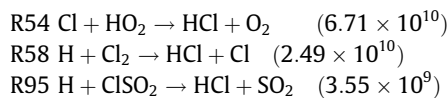
Their column rates are in parentheses in $\text{cm}^{-2} \text{ s}^{-1}$. (R50) and (R53) are opposite with almost equal rates. (R51) transforms odd hydrogen into odd chlorine, and this explains why the former is less abundant than the latter below 95 km.

Loss of HCl in reactions



$$\text{Total} \quad 9.94 \times 10^{10} \text{ cm}^{-2} \text{ s}^{-1}$$

is almost balanced by its production:



$$\text{Total} \quad 9.56 \times 10^{10} \text{ cm}^{-2} \text{ s}^{-1}.$$

The difference of $3.8 \times 10^9 \text{ cm}^{-2} \text{ s}^{-1}$ is released as a flow of SO₂Cl₂ into the lower atmosphere (Fig. 6). This flow exceeds by a factor of 2 the difference between the production of H₂O in (R51) HCl + OH and its loss by photolysis. (The factor of 2 is because two odd hydrogen species are formed by photolysis of H₂O.) Therefore the detailed balance between the H and Cl species can be easily checked using the column rates in Tables 4 and 5.

SO₂Cl₂ was mentioned but not calculated in Mills and Allen (2007) and is lacking in the other models of the middle atmosphere. It is the most abundant photochemical product of HCl in our model. Unfortunately, the SO₂Cl₂ chemistry in our model is based on assumptions and estimates. Its calculated mixing ratio is 8 ppb at 47 km and 30 ppb at 68 km. The value at 47 km is much larger than that in the kinetic model by Krasnopolsky (2007). That model does not include a flow of SO₂Cl₂ from the middle atmosphere.

The Cl₂ mixing ratio peaks at 70 km where it is equal to 22 ppb. Some differences between the rates and altitude distributions of (R50) and (R53) result in a deep minimum of H₂ at 72 km. Its mixing ratio is 4.5 ppb below 65 km and 23 ppb above 95 km (Fig. 6).

3.7. Odd nitrogen

Odd nitrogen chemistry is initiated by NO that is fixed at the lower boundary at 5.5 ppb observed by Krasnopolsky (2006a). Yung and DeMore (1982) developed a photochemical model where odd nitrogen chemistry dominated with a major cycle

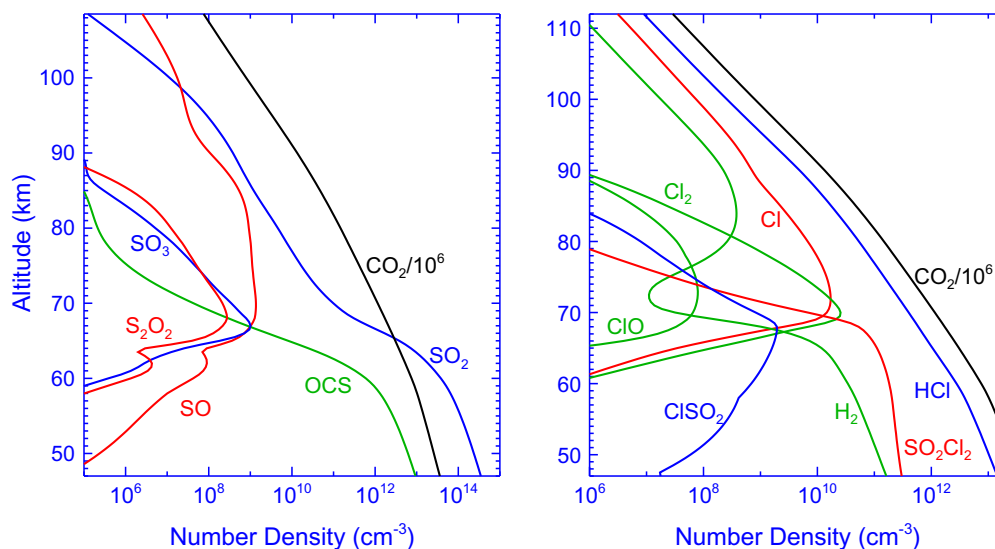
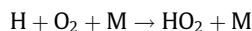


Fig. 6. Basic sulfur and chlorine species and H₂.

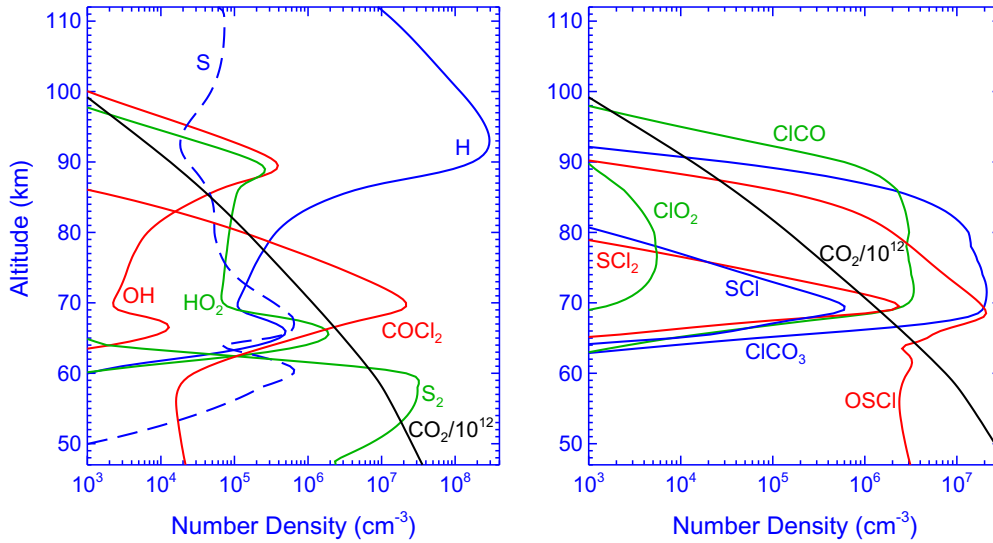
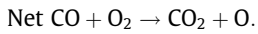
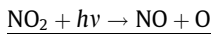
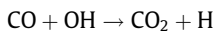
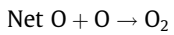
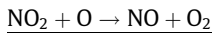
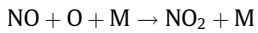


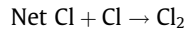
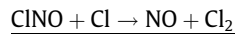
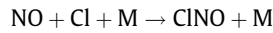
Fig. 7. Some minor species and radicals.



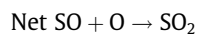
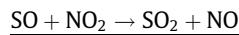
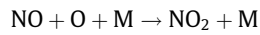
Their model had 30 ppb of NO and 500 ppb of H₂ at the lower boundary of 58 km that may be compared with 5.5 ppb and 4.5 ppb, respectively, in our model. Column rate of the key reaction of the cycle, (R80) NO + HO₂, is smaller than the CO₂ photolysis rate by a factor of 40, and this cycle is insignificant in our model. More important are the cycles



that provides a quarter of the O₂ production,



which is responsible for a third of the Cl₂ production, and



that compensates a quarter of the SO₂ photolysis. The calculated profiles of the odd nitrogen species are shown in Fig. 8. Overall, NO in the atmosphere of Venus is important as a convincing proof of lightning and an effective catalyst in the above cycles.

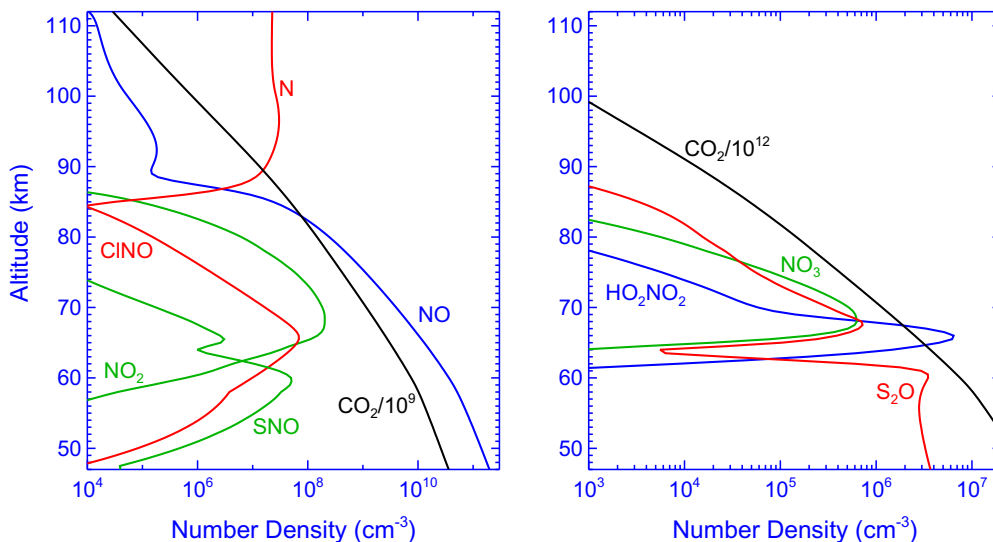


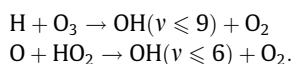
Fig. 8. Nitrogen species and S₂O.

3.8. O₂ and OH dayglow

The O₂^{*} = O₂(a¹Δ_g) density profile in Fig. 5 was calculated using the effective O₂(a¹Δ_g) yield of 0.7 by energy transfer from four metastable O₂ states formed by (R37) O + O + M in the CO₂ atmospheres (Krasnopolsky, 2011a). This profile results in the O₂ airglow at 1.27 μm with intensity of 0.85 megarayleigh (MR). Connes et al. (1979) observed the day and night airglows at 1.27 μm with intensities of 1.5 and 1.2 MR, respectively. The night-side mean airglow intensity is 0.52 MR in the Venus Express observations (Piccioni et al., 2009), and its scaling gives 0.52 * 1.5/1.2 = 0.65 MR for the dayglow intensity. The dayglow intensity in our model is between the observed and scaled values.

Discovery of the OH nightglow (Piccioni et al., 2008) was a significant achievement of the Venus Express mission. The observed OH nightglow is very different from that on the Earth and consists of the (1–0), (2–1), and (2–0) bands instead of ~50 bands up to $v' = 9$ in the terrestrial nightglow.

Krasnopolsky (2010a) developed a photochemical model for the nighttime atmosphere and nightglow on Venus. He considered two excitation processes



The standard excitation yields from Garcia Munoz et al. (2005) were adopted for the O₃ reaction, and yields of 0.3 for $v = 1, 2,$ and 3 in the HO₂ reaction were assumed based on Kaye (1988). Transition probabilities and quenching rate coefficients of the OH bands by CO₂ were taken from Garcia Munoz et al. (2005). Yields of the vibrational states of OH in the quenching by CO₂ are unknown and assumed equal to 0.4, 0.35, and 0.25 for $v = 0, 1, 2,$ respectively. The model gave intensities of 5.4 kR for the OH (1–0) band at 2.80 μm, 1.6 kR for the (2–1) band at 2.94 μm, and 0.7 kR for the (2–0) band at 1.43 μm, very similar to those observed (Piccioni et al., 2008; Soret et al., 2010). The O₃ reaction is responsible for ~95% of the observed OH nightglow.

Applying the above excitation scheme to the results of our current global-mean model, the expected OH airglow intensity is 17 kR, and the HO₂ reaction produces ~70% of the OH emission. The dayside ozone densities are depleted by photolysis, and this explains the smaller contribution of the H + O₃ reaction. The OH dayglow may be brighter in a dayside-mean model than that in our global-mean model by a factor of ~2, that is, ~30 kR. Though the OH dayglow is brighter than the nightglow by a factor of ~4, its detection is more difficult because of the sunlight conditions.

3.9. Minor species and radicals

Vertical profiles of almost all minor species and radicals are shown in Figs. 4–8. Combining these profiles with the column reaction rates and mean altitudes from Tables 4 and 5, it is possible to analyze a chemical balance of each species. Our model is open to the reader and provides rather detailed information on the subject.

3.10. Variations of species

Our model is based on the numerous input data, including the boundary conditions and the reaction rate coefficients. We discussed above the motivations for the chosen boundary conditions, and references to the laboratory studies of the reaction rate coefficients and other sources of the data are given in Tables 4 and 5. All these data are known with some uncertainties that make a huge number of degrees of freedom in our problem. Fortunately, variations of the model induced by the variations of the input data within their uncertainties are low except a few cases that will be considered in more detail (Table 8).

We have found that the model is extremely sensitive to small variations of eddy diffusion at the altitudes of the upper cloud layer (58–70 km). The variations are simulated by changing the eddy breakpoint by ±5 km from the value of 60 km in the basic model (Fig. 1). These small variations result in variations of the sulfur species above the clouds by a factor of ~30 (Fig. 3) and present a convincing proof that the observed variations of SO₂, SO, and OCS above the clouds are mostly caused by the atmospheric dynamics.

Variations with local time in the atmosphere rotating with a period of 4 days cannot be simulated by our steady-state model. However, some qualitative estimates may be done. For example, the SO₂ photolysis and formation of sulfuric acid cease at night, eddy diffusion drives SO₂ and H₂O up from the lower atmosphere, and the morning abundances of these species, say, near the cloud tops should be larger than the evening abundances, in accord with the observations (Krasnopolsky, 2010c). Comparison of this model with the nighttime photochemical model (Krasnopolsky, 2010a) may also be helpful in evaluations of the diurnal variations.

The model is also very sensitive to variations of the SO₂/H₂O ratio at the lower boundary. Variations of this ratio by 5% change the H₂O and SO_x abundances in the middle atmosphere by a factor of 2–7 (Table 8). Table 8 also includes a case with the standard CO velocity at the lower boundary that was considered in Section 3.1.

An estimate of a timescale for response of the atmospheric composition to the changes in dynamics and the SO₂/H₂O ratio near ~50 km may be made using the atmospheric scale height ~5 km and eddy diffusion of 10⁴ cm² s⁻¹ below 60 km; this gives $\tau = H^2/K \approx 1$ year. However, the SO₂ scale height reaches a minimum of ~1 km near the peak of the production of sulfuric acid at 66 km, where $K = 3 \times 10^4$ cm² s⁻¹; then $\tau \approx 4$ days, similar to the superrotation period.

4. Discussion

Formation of sulfuric acid near the cloud tops is a key feature of the Venus photochemistry. The atmosphere below the cloud tops is comparatively wet and rich in SO₂, and the bottleneck at 66 km greatly reduces the abundances of SO₂ and H₂O above the clouds. The losses of these species are balanced as 1:2, and any deviation from this ratio below the cloud tops changes drastically their abundances above the clouds. Eddy diffusion controls the SO₂ and H₂O flows that may come through the bottleneck, and its variations hugely affect the delivery of these species and the entire photochemistry above the clouds.

We put additional constraints to our model by using the lower boundary conditions from the kinetic model by Krasnopolsky (2007). While the overall agreement between the model and the observations is very good, there are some aspects that deserve discussion.

The O₂ column abundance in our model exceeds the observed upper limit (Trauger and Lunine, 1983; Krasnopolsky, 2006b) by an order of magnitude. We do not increase the CICO equilibrium constant to fit this limit, because this increase is not supported by the laboratory data. Therefore the problem remains unsolved.

SO₂ at the lower boundary is chosen in all models to fit the atmospheric composition above the clouds, and its value is 9.7 ppm in our model. There is a significant difference between this mixing ratio at 47 km in our model and a nearly constant value of 130 ppm throughout the lower atmosphere in the kinetic model (Krasnopolsky, 2007). This value was confirmed by the recent VEX/VIRTIS observations (Marcq et al., 2008). There are no processes that could significantly deplete SO₂ in that model. Evidently

our understanding of the sulfur chemistry near the lower cloud boundary on Venus is incomplete.

Production of the aerosol sulfur and its flux into the lower atmosphere is very low, $5.5 \times 10^8 \text{ cm}^{-2} \text{ s}^{-1}$. It was adopted at $5 \times 10^{11} \text{ cm}^{-2} \text{ s}^{-1}$ in the basic model for the lower atmosphere. Krasnopolsky (2007) also calculated a model with no sulfur flux at 47 km (see Table 4 in that paper), and that model is in reasonable agreement with the observations as well.

The calculated fluxes of CO and sulfuric acid in our model are smaller than those adopted in Krasnopolsky (2007) and Krasnopolsky and Pollack (1994) by a factor of 3. This difference between the models is neither large nor negligible.

The OCS mixing ratio of 260 ppb taken as the lower boundary condition in our model from Krasnopolsky (2007) leads to agreement between the current model and the observations at 65 km. That was unexpected for us, because OCS was not fixed at 47 km in Krasnopolsky (2007) and we do not have tools in our model to fit the observations. Our model does not require an abundant OCS of 1.5 ppm at 58 km that was adopted by Zhang et al. (2012) to fit the observations.

Main photochemical products that are delivered into the lower atmosphere are CO, $\text{H}_2\text{SO}_4 \cdot \text{H}_2\text{O}$, and SO_2Cl_2 , and their fluxes are 6.4×10^{11} , 5.7×10^{11} , and $1.9 \times 10^9 \text{ cm}^{-2} \text{ s}^{-1}$, respectively. These fluxes are compensated by the upward flows of CO_2 , SO_2 , H_2O , OCS, and HCl from the lower atmosphere that are equal to 6.2×10^{11} , 5.5×10^{11} , 1.2×10^{12} , 2×10^{10} , and $3.9 \times 10^9 \text{ cm}^{-2} \text{ s}^{-1}$, respectively. Therefore the chemically neutral CO_2 and SO_2 are converted in the middle atmosphere and returned to the lower atmosphere as the reduced CO and oxidizing SO_3 in H_2SO_4 . The delivered fluxes of CO, H_2SO_4 , and SO_2Cl_2 are reprocessed by thermochemistry in the lower atmosphere, and the atmospheric system may be closed, that is, generally does not form any deposits and does not require outgassing from the interior. However, some gas exchange with the surface rocks is certainly not ruled out by our models.

5. Conclusions

This work is intended to respond to the recent findings in the Venus atmosphere from the Venus Express and ground-based sub-millimeter and infrared observations. The developed photochemical model is extended down to 47 km to use the data of the kinetic model for the lower atmosphere (Krasnopolsky, 2007) as the boundary conditions and for comparison of the results. The altitude step is reduced from 2 km in all previous models to 0.5 km, with a significant improvement of the numerical accuracy. Effects of the NUV absorber are accounted for using the detailed photometric data from Venera 14. The H_2O profile is not fixed but calculated in the model. The model involves odd nitrogen and OCS chemistries based on the detected NO and OCS abundances. The number of the reactions is significantly reduced by removing of unimportant processes. Column rates for all reactions are given for the basic model, and a balance of production and loss may be analyzed in detail for each species.

The calculated vertical profiles of CO, H_2O , HCl, SO_2 , SO, and OCS generally agree with the existing observational data; some differences are briefly discussed. The calculated O_2 dayglow at 1.27 μm agrees with the observations as well. The OH dayglow is ~ 30 kR, brighter than the OH nightglow by a factor of ~ 4 . The $\text{H} + \text{O}_3$ process dominates in the nightglow excitation and $\text{O} + \text{HO}_2$ in the dayglow.

The model is extremely sensitive to small variations of eddy diffusion near 60 km. These variations induce variations of SO_2 , SO, and OCS at and above the cloud tops within a factor of ~ 30 . Variations of the $\text{SO}_2/\text{H}_2\text{O}$ ratio at the lower boundary have similar but

weaker effect (variations within a factor of ~ 4 are induced by changes of $\text{SO}_2/\text{H}_2\text{O}$ by $\pm 5\%$). Therefore the observed variations of sulfur species and water vapor in the mesosphere originate from minor variations of the atmospheric dynamics at the cloud layer and do not require volcanism.

NO initiates cycles that are responsible for production of a quarter of O_2 , SO_2 , and Cl_2 in the atmosphere. However, the H_2 abundance is low, and the CO_2 recombination via the $\text{NO} + \text{HO}_2$ cycle proposed by Yung and DeMore (1982) is insignificant.

Consumption of CO_2 , SO_2 , H_2O , and HCl from the lower atmosphere and return of CO, H_2SO_4 , and SO_2Cl_2 is the net effect of photochemistry in the middle atmosphere. These processes may be balanced by thermochemistry in the lower atmosphere even without outgassing from the interior, though the latter is not ruled out by our models. Some differences between the model and observations and the previous models are briefly discussed.

Acknowledgments

This work is supported by the Russian Government grant to the Moscow Institute of Physics and Technology and V.A. Krasnopolsky.

References

- Abbatt, J.P.D., Toohey, D.W., Fenter, F.F., Stevens, P.S., Brune, W.H., Anderson, J.G., 1989. Kinetics and mechanism of $\text{X} + \text{ClNO} \rightarrow \text{XCl} + \text{NO}$ ($\text{X} = \text{Cl}, \text{F}, \text{Br}, \text{OH}, \text{O}, \text{N}$) from 220 to 450 K. Correlation of reactivity and activation energy with electron affinity of X. *J. Phys. Chem.* 93, 1022–1029.
- Adusei, G.Y., Fontijn, A., 1994. Experimental studies of Cl-atom reactions at high temperatures: $\text{Cl} + \text{H}_2 \rightarrow \text{HCl} + \text{H}$ from 291 to 1283 K. *Symp. Int. Combust. Proc.* 25, 801–808.
- Allen, M., Frederick, J.E., 1982. Effective photodissociation cross sections for molecular oxygen and nitric oxide in the Schumann–Runge bands. *J. Atmos. Sci.* 39, 2066–2075.
- Atkinson, R. et al., 2007. Evaluated kinetic and photochemical data for atmospheric chemistry: Volume III – Gas phase reactions of inorganic halogens. *Atmos. Chem. Phys.* 7, 981–1191.
- Bahou, M., Chung, C.Y., Lee, Y.P., Cheng, B.M., Yung, Y.L., Lee, L.C., 2001. Absorption cross sections of HCl and DCl at 135–232 nanometers: Implications for photodissociation on Venus. *Astrophys. J.* 559, L179–L182.
- Bailey, J., Meadows, V.S., Chamberlain, S., Crisp, D., 2008. The temperature of the Venus mesosphere from O_2 ($a^1\Delta_g$) airglow observations. *Icarus* 197, 247–259.
- Baulch, D.L., Duxbury, J., Grant, S.J., Montague, D.C., 1981. Evaluated kinetic data for high temperature reactions. Volume 4 homogeneous gas phase reactions of halogen- and cyanide-containing species. *J. Phys. Chem. Ref. Data.* 1–721.
- Bedjanian, Y., Riffault, V., Le Bras, G., 2001. Kinetics and mechanism of the reaction of OH with ClO. *Int. J. Chem. Kinet.* 33, 587–599.
- Belyaev, D. et al., 2008. First observations of SO_2 above Venus clouds by means of solar occultation in the Infrared. *J. Geophys. Res.* 113, E00B25. doi:10.1029/2008JE003143.
- Belyaev, D. et al., 2012. Vertical profiling of SO_2 and SO above Venus' clouds by SPICAV/SOIR solar occultations. *Icarus*, in press.
- Berho, F., Rayez, M.-T., Lesclaux, R., 1999. UV absorption spectrum and self-reaction kinetics of the cyclohexadienyl radical, and stability of a series of cyclohexadienyl-type radicals. *J. Phys. Chem. A* 103, 5501–5509.
- Bertaux, J.L. et al., 2007. A warm layer in Venus' cryosphere and high-altitude measurements of HF, HCl, H_2O and HDO. *Nature* 450, 646–649.
- Bezard, B., Fedorova, A., Bertaux, J.L., Rodin, A., Korablev, O., 2011. The 1.10- and 1.18- μm nightside windows of Venus observed by SPICAV-IR aboard Venus Express. *Icarus* 216, 173–183.
- Billmers, R.I., Smith, A.I., 1991. Ultraviolet-visible absorption spectra of equilibrium sulfur vapor: Molar absorptivity spectra of S_3 and S_4 . *J. Phys. Chem.* 95, 4242–4245.
- Bjoraker, G.L., Larson, H.P., Mumma, M.J., Timmermann, R., Montani, J.L., 1992. Airborne observations of the gas composition of Venus above the cloud tops: Measurements of H_2O , HDO, HF and the D/H and $^{18}\text{O}/^{16}\text{O}$ isotope ratios. *Bull. Amer. Astron. Soc.* 24, 995 (abstract).
- Burkholder, J.B., McKeen, S., 1997. UV absorption cross sections for SO_3 . *Geophys. Res. Lett.* 24, 3201–3204.
- Burns, W.G., Dainton, F.S., 1952. The rate constants of the reactions of nitrosyl chloride with chlorine atoms and COCl radicals. *Trans. Faraday Soc.* 48, 52–62.
- Campbell, I.M., Thrush, B.A., 1966. Behaviour of carbon dioxide and nitrous oxide in active nitrogen. *Trans. Faraday Soc.* 62, 3366–3374.
- Cheng, B.M. et al., 1999. Photo-induced fractionation of water isotopomers in the martian atmosphere. *Geophys. Res. Lett.* 26, 3657–3660.
- Christensen, L.E., Okumura, M., Sander, S.P., Friedl, R.R., Miller, C.E., Sloan, J.J., 2004. Measurements of the rate constant of $\text{HO}_2 + \text{NO}_2 + \text{N}_2 \rightarrow \text{HO}_2\text{NO}_2 + \text{N}_2$ using

- near-infrared wavelength-modulation spectroscopy and UV-visible absorption spectroscopy. *J. Phys. Chem. A* 108, 80–91.
- Chung, K., Calvert, J.G., Bottenheim, J.W., 1975. The photochemistry of sulfur dioxide excited within its first allowed band (3130 Å) and the “forbidden” band (3700–4000 Å). *Int. J. Chem. Kinet.* 7, 161–182.
- Clancy, R.T., Sandor, B.J., Moriarty-Schieven, G., 2012. Thermal structure and CO distribution for the Venus mesosphere/lower thermosphere: 2001–2009 inferior conjunction sub-millimeter CO absorption line observations. *Icarus*, in press.
- Clark, T.C., Clyne, M.A.A., Stedman, D.H., 1966. Mechanism of formation of triatomic molecules in atomic combination reactions. Part 1. Formation of ClNO and ClCO in reactions of atomic chlorine. *Trans. Faraday Soc.* 62, 3354–3365.
- Connes, P., Connes, J., Kaplan, L.D., Benedict, W.S., 1968. Carbon monoxide in the Venus atmosphere. *Astrophys. J.* 152, 731–743.
- Connes, P., Noxon, J.F., Traub, W.A., Carleton, N.P., 1979. O₂ (¹Δ) emission in the day and night airglow of Venus. *Astrophys. J.* 233, L29–L32.
- Cottini, V., Ignatiev, N.I., Piccioni, G., Drossart, P., Grassi, D., Markiewicz, W.J., 2012. Water vapor near the cloud tops of Venus from Venus Express/VIRTIS dayside data. *Icarus*, in press.
- Craven, W., Murrell, J.N., 1987. Trajectory studies of S + O₂ and O + S₂ collisions. *J. Chem. Soc. Faraday Trans.* 2, 83, 1733–1741.
- Crisp, D., 1986. Radiative forcing of the Venus mesosphere I: Solar fluxes and heating rates. *Icarus* 67, 484–514.
- Dalgarno, A., Babb, J.F., Sun, Y., 1992. Radiative association in planetary atmospheres. *Planet. Space Sci.* 40, 243–246.
- Du, S.Y., Francisco, J.S., Shepler, B.C., Peterson, K.A., 2008. Determination of the rate constant for sulfur recombination by quasiclassical trajectory calculations. *J. Chem. Phys.* 128, 204306, doi:10.1063/1.2919569.
- Ekonomov, A.P., Moshkin, B.E., Moroz, V.I., Golovin, Yu.M., Gnedykh, V.I., Grigoriev, A.V., 1983. UV photometry at the Venera 13 and 14 landing probes. *Cosmic Res.* 21, 194–206.
- Enami, S., Hoshino, Y., Ito, Y., Hashimoto, S., Kawasaki, M., Wallington, T.J., 2006. Kinetic study of the ClOO plus NO reaction using cavity ring-down spectroscopy. *J. Phys. Chem. A* 110, 3546–3551.
- Encrenaz, Th., Lellouch, E., Cernicharo, J., Paubert, G., Gulkis, S., Spilker, T., 1995. The thermal profile and water abundance in the Venus mesosphere from H₂O and HDO millimeter observations. *Icarus* 117, 162–172.
- Esposito, L.W., Copley, M., Eckert, R., Gates, L., Stewart, A.I.F., Worden, H., 1988. Sulfur dioxide at the Venus cloud tops, 1978–1986. *J. Geophys. Res.* 93, 5267–5276.
- Esposito, L.W., Bertaux, J.-L., Krasnopolsky, V., Moroz, V.I., Zasova, L.V., 1997. Chemistry of lower atmosphere and clouds. In: Bougher, S.W., Hunten, D.M., Phillips, R.J. (Eds.), *Venus II: Geology, Geophysics, Atmosphere, and Solar Wind Environment*. University of Arizona Press, Tucson, pp. 415–458.
- Fair, R.W., Thrush, B.A., 1969. Mechanism of S₂ chemiluminescence in the reaction of hydrogen atoms with hydrogen sulphide. *Trans. Faraday Soc.* 65, 1208–1218.
- Fedorova, A. et al., 2008. HDO and H₂O vertical distributions and isotopic ratio in the Venus mesosphere by solar occultation at infrared spectrometer on board Venus Express. *J. Geophys. Res.* 113, E00B22.
- Fernandez, A., Goumri, A., Fontijn, A., 1998. Kinetics of the reactions of N(⁴S) atoms with O₂ and CO₂ over wide temperature ranges. *J. Phys. Chem. A* 102, 168–172.
- Fink, U., Larson, H.P., Kuiper, G.P., Poppe, R.F., 1972. Water vapor in the atmosphere of Venus. *Icarus* 17, 617–631.
- Frost, M.J., Sharkey, P., Smith, I.W.M., 1993. Reaction between OH (OD) radicals and CO at temperatures down to 80 K: Experiment and theory. *J. Phys. Chem.* 97, 12254–12259.
- García Muñoz, A., McConnell, J.C., McDade, I.C., Melo, S.M.L., 2005. Airglow on Mars: Some model expectations for the OH Meinel bands and the O₂ IR atmospheric band. *Icarus* 176, 75–95.
- García Muñoz, A., Mills, F.P., Piccioni, G., Drossart, P., 2009a. The near-infrared nitric oxide nightglow in the upper atmosphere of Venus. *PNAS* 106, 985–988.
- García Muñoz, A., Mills, F.P., Slangier, T.G., Piccioni, G., Drossart, P., 2009b. Visible and near-infrared nightglow of molecular oxygen in the atmosphere of Venus. *J. Geophys. Res.* 114, E12002.
- Gerard, J.C., Cox, C., Saglam, A., Bertaux, J.L., Villard, E., Nehme, C., 2008. Limb observations of the ultraviolet nitric oxide nightglow with SPICAV on board Venus Express. *J. Geophys. Res.* 113, E00B03.
- Goumri, A., Shao, D.D., Marshall, P., 2004. Reaction kinetics of the addition of atomic sulfur to nitric oxide. *J. Chem. Phys.* 121, 9999–10005.
- Gurwell, M.A., Melnick, G.J., Tolls, V., Bergin, E.A., Patten, B.M., 2007. SWAS observations of water vapor in the Venus mesosphere. *Icarus* 188, 288–304.
- Herron, J.T., 1988. Evaluated chemical kinetic data for the reactions of atomic oxygen O(³P) with saturated organic compounds in the gas phase. *J. Phys. Chem. Ref. Data*, 17.
- Herron, J.T., Huie, R.E., 1980. Rate constants at 298 K for the reactions SO + SO + M → (SO)₂ + M and SO + (SO)₂ → SO₂ + S₂O. *Chem. Phys. Lett.* 76, 322–324.
- Hewitt, A.D., Brahan, K.M., Boone, G.D., Hewitt, S.A., 1996. Kinetics and mechanism of the Cl + CO reaction in air. *Int. J. Chem. Kinet.* 28, 763–771.
- Ignatiev, N.I., Moroz, V.I., Zasova, L.V., Khatuntsev, I.V., 1999. Water vapor in the middle atmosphere of Venus: An improved treatment of the Venera 15 IR spectra. *Planet. Space Sci.* 47, 1061–1075.
- Inn, E.C.Y., 1974. Rate of recombination of oxygen atoms and CO at temperatures below ambient. *J. Chem. Phys.* 61, 1589–1590.
- Irwin, P.G.J., de Kok, R., Nagrao, A., Tsang, C.C.C., Wilson, C.F., Drossart, P., Piccioni, G., Grassi, D., Taylor, F.W., 2008. Spatial variability of carbon monoxide in Venus' mesosphere from Venus Express/visible and infrared thermal imaging spectrometer measurements. *J. Geophys. Res.* 113, E00B01.
- Jacob, A., Winkler, C.A., 1972. Kinetics of the reactions of oxygen atoms and nitrogen atoms with sulfur trioxide. *J. Chem. Soc. Faraday Trans.* 1, 68, 2077–2082.
- Kaye, J.A., 1988. On the possible role of the reaction O + HO₂ → OH + O₂ in OH airglow. *J. Geophys. Res.* 93, 285–288.
- Keating, G.M. et al., 1985. Models of Venus neutral upper atmosphere: Structure and composition. *Adv. Space Res.* 5, 117–171.
- Koukouli, M.E., Irwin, P.G.J., Taylor, F.W., 2005. Water vapor abundance in Venus' middle atmosphere from Pioneer Venus OIR and Venera 15 FTS measurements. *Icarus* 173, 84–99.
- Krasnopolsky, V.A., 1980. Veneras 9 and 10: Spectroscopy of scattered radiation in overcloud atmosphere. *Cosmic Res.* 18, 899–906.
- Krasnopolsky, V.A., 1983. Venus spectroscopy in the 3000–8000 Å region by Veneras 9 and 10. In: Hunten, D.M., Colin, L., Donahue, T.M., Moroz, V.I. (Eds.), *Venus Univ. Arizona Press*, pp. 459–483.
- Krasnopolsky, V.A., 1985. Chemical composition of Venus clouds. *Planet. Space Sci.* 33, 109–117.
- Krasnopolsky, V.A., 1986. *Photochemistry of the Atmospheres of Mars and Venus*. Springer-Verlag, New York.
- Krasnopolsky, V.A., 1995. Uniqueness of a solution of a steady-state photochemical problem: Applications to Mars. *J. Geophys. Res. (Planets)* 100, 3263–3276.
- Krasnopolsky, V.A., 2006a. A sensitive search for nitric oxide in the lower atmospheres of Venus and Mars: Detection on Venus and upper limit for Mars. *Icarus* 182, 80–91.
- Krasnopolsky, V.A., 2006b. Chemical composition of Venus atmosphere and clouds: Some unsolved problems. *Planet. Space Sci.* 54, 1352–1359.
- Krasnopolsky, V.A., 2007. Chemical kinetic model for the lower atmosphere of Venus. *Icarus* 191, 25–37.
- Krasnopolsky, V.A., 2008. High-resolution spectroscopy of Venus: Detection of OCS, upper limit to H₂S, and latitudinal variations of CO and HF in the upper cloud layer. *Icarus* 197, 377–385.
- Krasnopolsky, V.A., 2010a. Venus night airglow: Ground-based detection of OH, observations of O₂ emissions, and photochemical model. *Icarus* 207, 17–27.
- Krasnopolsky, V.A., 2010b. Spatially-resolved high-resolution spectroscopy of Venus. 1. Variations of CO₂, CO, HF, and HCl at the cloud tops. *Icarus* 208, 539–547.
- Krasnopolsky, V.A., 2010c. Spatially-resolved high-resolution spectroscopy of Venus. 2. Variations of HDO, OCS, and SO₂ at the cloud tops. *Icarus* 209, 314–322.
- Krasnopolsky, V.A., 2011a. Excitation of the oxygen nightglow on the terrestrial planets. *Planet. Space Sci.* 59, 754–766.
- Krasnopolsky, V.A., 2011b. Vertical profile of H₂SO₄ vapor at 70–110 km and some related problems. *Icarus* 215, 197–203.
- Krasnopolsky, V.A., Cruikshank, D.P., 1999. Photochemistry of Pluto's atmosphere and ionosphere near perihelion. *J. Geophys. Res.* 104, 21979–21996.
- Krasnopolsky, V.A., Parshv, V.A., 1981. Chemical composition of the atmosphere of Venus. *Nature* 282, 610–612.
- Krasnopolsky, V.A., Parshv, V.A., 1983. Photochemistry of the Venus atmosphere. In: Hunten, D.M., Colin, L., Donahue, T.M., Moroz, V.I. (Eds.), *Venus Univ. Arizona Press, Tucson*, pp. 431–458.
- Krasnopolsky, V.A., Pollack, J.B., 1994. H₂O–H₂SO₄ system in Venus' clouds and OCS, CO, and H₂SO₄ profiles in Venus' troposphere. *Icarus* 109, 58–78.
- Lafferty, W.J., Solodov, A.M., Lugez, C.L., Fraser, G.T., 1998. Rotational line strengths and self-pressure broadening coefficients for the 1.27-μm, a¹Δ_g – X²Σ_g, v = 0–0 band of O₂. *Appl. Opt.* 37, 2264–2270.
- Lane, W.A., Optsbaum, R., 1983. High altitude Venus haze from Pioneer Venus limb scans. *Icarus* 54, 48–58.
- Lellouch, E., Goldstein, J.J., Rosenqvist, J., Bougher, S.W., Paubert, G., 1994. Global circulation, thermal structure, and carbon monoxide distribution in Venus' mesosphere in 1991. *Icarus* 110, 315–339.
- Lewis, B.R., Carver, J.H., 1983. Temperature dependence of the carbon dioxide photoabsorption cross section between 1200 and 1970 Å. *J. Quant. Spectr. Rad. Trans.* 30, 297–309.
- Loverjoy, E.R., Hanson, D.R., Huey, L.G., 1996. Kinetics and products of the gas-phase reaction of SO₃ with water. *J. Phys. Chem.* 100, 19911–19916.
- Lu, C.W., Wu, Y.J., Lee, Y.P., Zhu, R.S., Lin, M.C., 2003. Experiments and calculations on rate coefficients for pyrolysis of SO₂ and the reaction O plus SO at high temperatures. *J. Phys. Chem. A* 107, 11020–11029.
- Lu, C.W., Wu, Y.J., Lee, Y.P., Zhu, R.S., Lin, M.C., 2006. Experimental and theoretical investigation of rate coefficients of the reaction S(³P) + OCS in the temperature range of 298–985 K. *J. Chem. Phys.*, 125.
- Lyons, J.R., 2008. An estimate of the equilibrium speciation of sulfur vapor over solid sulfur and implications for planetary atmospheres. *J. Sulfur Chem.* 29, 269–279.
- Manatt, S.L., Lane, A.L., 1993. A compilation of the absorption cross sections of SO₂ from 106 to 403 nm. *J. Quant. Spectr. Rad. Tran.* 50, 267–276.
- Marq, E., Bezard, B., Drossart, P., Piccioni, G., Reess, M., Henry, F., 2008. A latitudinal survey of CO, OCS, H₂O, and SO₂ in the lower atmosphere of Venus: Spectroscopic studies using VIRTIS-H. *J. Geophys. Res.* 113, E00B07.
- Marq, E., Belyaev, D., Montmessin, F., Fedorova, A., Bertaux, J.L., Vandaele, A.C., Neefs, E., 2011. An investigation of the SO₂ content of the venusian mesosphere using SPICAV-UV in nadir mode. *Icarus* 211, 58–69.
- Marsden, C.J., Smith, B.U., 1990. An *ab initio* study of many isomers of S₂O₂. A combined theoretical and experimental analysis of the harmonic force field and molecular structure of its *cis*-planar OSSO. *Chem. Phys.* 141, 335–353.

- Martinez, R.I., Herron, J.T., 1983. Methyl thiirane: Kinetic gas-phase titration of sulfur atoms in S_xO_y systems. *Int. J. Chem. Kinet.* 15, 1127–1132.
- Mills, K.C., 1974. Thermodynamic Data for Inorganic Sulfides, Selenides, and Tellurides. Butterworths, London.
- Mills, F.P., 1998. I. Observations and Photochemical Modeling of the Venus Middle Atmosphere. II. Thermal Infrared Spectroscopy of Europa and Callisto. Ph.D. thesis. California Institute of Technology.
- Mills, F.P., Allen, M., 2007. A review of selected issues concerning the chemistry in Venus' middle atmosphere. *Planet. Space Sci.* 55, 1729–1740.
- Molina, L.T., Lamb, J.J., Molina, M.J., 1981. Temperature dependent UV absorption cross sections for carbonyl sulfide. *Geophys. Res. Lett.* 8, 1008–1011.
- Moses, J.I., Zolotov, M.Yu., Fegley, Jr., B., 2002. Photochemistry of a volcanically driven atmosphere of Io: Sulfur and oxygen species from a Pele-type eruption. *Icarus* 156, 76–106.
- Murrells, T.P., 1988a. Elementary reactions of the SCl radical. Part 1. Rate constants and mechanisms of the reactions $Cl + C_2H_4S \rightarrow SCl + C_2H_4$, $SCl + SCl \rightarrow$ products and $SCl + Cl_2 \rightarrow SCl_2 + Cl$. *J. Chem. Soc. Faraday Trans. 2*, 67–83.
- Murrells, T.P., 1988b. Elementary reactions of the SCl radical. Part 2. Rate constants and mechanisms of the reactions of SCl with NO_2 , NO , O_2 , $O(^3P)$ and $N(^4S)$. *J. Chem. Soc. Faraday Trans. 2*, 85–94.
- Naidoo, J., Goumri, A., Marshall, P., 2005. A kinetic study of the reaction of atomic oxygen with SO_2 . *Proc. Combust. Inst.* 30, 1219–1225.
- Nair, H., Allen, M., Anbar, A.D., Yung, Y.L., Clancy, R.T., 1994. A photochemical model of the martian atmosphere. *Icarus* 111, 124–150.
- Nicholas, J.E., Amodio, C.A., Baker, M.J., 1979. Kinetics and mechanism of the decomposition of H_2S , CH_3SH and $(CH_3)_2S$ in a radio-frequency pulse discharge. *J. Chem. Soc. Faraday Trans. 1*, 75, 1868–1875.
- Nicovich, J.M., Kreutter, K.D., Wine, P.H., 1990. Kinetics and thermochemistry of ClCO formation from the $Cl + CO$ association reaction. *J. Chem. Phys.* 92, 3539–3544.
- Ohtsuki, S. et al., 2008. Distribution of the Venus 1. 27- μm O_2 airglow and rotational temperature. *Planet. Space Sci.* 56, 1391–1398.
- Parkinson, W.H., Rufus, J., Yoshino, K., 2003. Absolute absorption cross section measurements of CO_2 in the wavelength region 163–200 nm and the temperature dependence. *Chem. Phys.* 290, 251–256.
- Pernice, H., Garcia, P., Willner, H., Francisco, J.S., Mills, F.P., Allen, M., Yung, Y.L., 2004. Laboratory evidence for a key intermediate in the Venus atmosphere: Peroxychloroformyl radical. *PNAS* 101, 14007–14010.
- Phillips, L.F., 1981. Absolute absorption cross sections for SO between 190 and 235 nm. *J. Phys. Chem.* 85, 3994–4000.
- Piccioni, G. et al., 2008. First detection of hydroxyl in the atmosphere of Venus. *Astron. Astrophys.* 483, L29–L33.
- Piccioni, G., Zasova, L., Migliorini, A., Drossart, P., Shakun, A., Garcia Munoz, A., Mills, F.P., Cardesin-Moinelo, A., 2009. Near-IR oxygen nightglow observed by VIRTIS in the Venus upper atmosphere. *J. Geophys. Res.* 114, E00B38.
- Pollack, J.B. et al., 1993. Near-infrared light from Venus' nightside – A spectroscopic analysis. *Icarus* 103, 1–42.
- Prahlad, V., Kumar, V., 1997. Temperature dependence of photoabsorption cross-sections of sulfur dioxide at 188–220 nm. *J. Quant. Spectr. Rad. Tran.* 57, 719–723.
- Prinn, R.G., 1971. Photochemistry of HCl and other minor constituents in the atmosphere of Venus. *J. Atmos. Sci.* 28, 1058–1068.
- Robertson, R., Smith, G.P., 2006. Temperature dependence of $O + OH$ at 136–377 K using ozone photolysis. *J. Phys. Chem. A* 110, 6673–6679.
- Sander, S.P. et al., 2002. Chemical Kinetics and Photochemical Data for Use in Stratospheric Modeling, Evaluation number 14. JPL Publication 02–25.
- Sander, S.P. et al., 2011. Chemical Kinetics and Photochemical Data for Use in Atmospheric Studies, Evaluation Number 17. JPL Publication 10–6.
- Sandor, B.J., Clancy, R.T., 2005. Water vapor variations in the Venus mesosphere from microwave spectra. *Icarus* 177, 129–143.
- Sandor, B.J., Clancy, R.T., Moriarty-Schieven, G., Mills, F.P., 2010. Sulfur chemistry in the Venus mesosphere from SO_2 and SO microwave spectra. *Icarus* 208, 49–60.
- Sandor, B.J., Clancy, R.T., Moriarty-Schieven, G., 2012. Upper limits for H_2SO_4 in the mesosphere of Venus. *Icarus*, in press.
- Seiff, A. et al., 1985. Models of the structure of the atmosphere of Venus from the surface to 100 kilometers altitude. *Adv. Space Res.* 5, 3–58.
- Shemansky, D.E., 1972. CO_2 extinction coefficient 1700–3000 Å. *J. Chem. Phys.* 56, 1582–1587.
- Singleton, D.L., Cvetanovic, R.J., 1988. Evaluated chemical kinetic data for the reactions of atomic oxygen $O(^3P)$ with sulfur containing compounds. *J. Phys. Chem. Ref. Data*, 17.
- Slanger, T.G., Huestis, D.L., Cosby, P.C., Chanover, N.J., Bida, T.A., 2006. The Venus nightglow ground-based observations and chemical mechanisms. *Icarus* 182, 1–9.
- Smith, G.P., Robertson, R., 2008. Temperature dependence of oxygen atom recombination in nitrogen after ozone photolysis. *Chem. Phys. Lett.* 458, 6–10.
- Soret, L., Gérard, J.-C., Piccioni, G., Drossart, P., 2010. Venus OH nightglow distribution based on VIRTIS limb observations from Venus Express. *Geophys. Res. Lett.* 37 (6), L06805.
- Thomas, J.H., Woodman, G.R., 1967. Gas-phase reactions between carbon monoxide, chlorine and nitrogen dioxide. *Trans. Faraday Soc.* 63, 2728–2736.
- Trauger, J.T., Lunine, J.I., 1983. Spectroscopy of molecular oxygen in the atmospheres of Venus and Mars. *Icarus* 55, 272–281.
- Uthman, A.P., Demlein, P.J., Allston, T.D., Withiam, M.C., McClements, M.J., Takacs, G.A., 1978. Photoabsorption spectra of gaseous methyl bromide, ethylene dibromide, nitrosyl bromide, thionyl chloride, and sulfuryl chloride. *J. Phys. Chem.* 82, 2252–2257.
- Vandaele, A.C. et al., 2008. Composition of the Venus mesosphere measured by solar occultation at infrared on board Venus Express. *J. Geophys. Res.* 113, E00B23.
- Von Zahn, U., Fricke, K.H., Hunten, D.M., Krankowsky, D., Mauersberger, K., Nier, A.O., 1980. The upper atmosphere of Venus during morning conditions. *J. Geophys. Res.* 85, 7829–7840.
- Weng, C.-J., Ho, T.-I., Su, T.-M., 1987. Laser photolysis study of the recombination reactions of atomic chlorine in inert gases. *J. Phys. Chem.* 91, 5235.
- Wennberg, P.O., Anderson, J.G., Weisenstein, D.K., 1994. Kinetics of reactions of ground state nitrogen atoms ($^4S_{3/2}$) with NO and NO_2 . *J. Geophys. Res.* 99, 18839–18846.
- Widman, R.P., DeGraff, B.A., 1973. On the gas-phase recombination of chlorine atoms. *J. Phys. Chem.* 77, 1325–1328.
- Wine, P.H., Nicovich, J.M., Ravishankara, A.R., 1985. Kinetics of the reactions of $O(^3P)$ and $O(^1D)$ with Cl_2 . *J. Phys. Chem.* 89, 3914–3918.
- Woo, R., Ishimaru, A., 1981. Eddy diffusion coefficient for the atmosphere of Venus from radio scintillation measurements. *Nature* 289, 383–384.
- Woods, T.N. et al., 1996. Validation of the UARS solar ultraviolet irradiances: Comparison with the ATLAS 1 and 2 measurements. *J. Geophys. Res.* 101, 9541–9569.
- Yung, Y.L., DeMore, W.B., 1982. Photochemistry of the stratosphere of Venus: Implications for atmospheric evolution. *Icarus* 51, 199–247.
- Zabel, F., 1995. Unimolecular decomposition of peroxy nitrates. *Z. Phys. Chem. (Munich)* 188, 119–142.
- Zasova, L.V., Krasnopolsky, V.A., Moroz, V.I., 1981. Vertical distribution of SO_2 in the upper cloud layer and origin of the UV absorption. *Adv. Space Res.* 1 (#1), 13–16.
- Zhang, X., Liang, M.C., Montmessin, F., Bertaux, J.L., Parkinson, C., Yung, Y.L., 2010. Photolysis of sulphuric acid as the source of sulphur oxides in the mesosphere of Venus. *Nat. Geosci.* 3, 834–837.
- Zhang, X., Liang, M.C., Mills, F.P., Belyaev, D.A., Yung, Y.L., 2012. Sulfur chemistry in the middle atmosphere of Venus. *Icarus*, in press.